

# Community Radiative Transfer Model for Air Quality Studies

Quanhua Liu and Cheng-Hsuan Lu

## 1 Introduction

Community Radiative Transfer Model (CRTM) (Han et al. 2006), developed at the Joint Center for Satellite Data Assimilation, has been operationally supporting satellite radiance assimilation for weather forecasting and Earth observation space programs. The CRTM has been supporting the Geostationary satellite (GOES)—R and Joint Polar Satellite System (JPSS) Suomi NPP missions for instrument calibration, validation, monitoring long-term trending, and satellite products using a retrieval approach (Liu and Boukabara 2014). At the both National Oceanic and Atmospheric Administration (NOAA) National Centers for Environmental Prediction (NCEP) and the NOAA National Environmental Satellite, Data, and Information Service (NESDIS) satellite radiance monitoring systems, the CRTM model is applied to simulate satellite observations. The CRTM has been used to assimilate Moderate Resolution Imaging Spectroradiometer (MODIS) aerosol optical depth for air quality forecasting (Liu et al. 2011). Similar to weather forecasting, the air quality forecasting is governed by air fluid dynamic equations based on aerosol sources and the emission of ozone, carbon monoxide, ammonia, and other gases as well as their chemical reactions. Suspended particulate matter

---

Q. Liu (✉)

Center for Satellite Applications and Research, National Oceanic and Atmospheric Administration, 5830 University Research Court, College Park, MD 20740, USA  
e-mail: Quanhua.Liu@noaa.gov

C.-H. Lu

Atmospheric Sciences Research Center, State University of New York, 1400 Washington Ave, Albany, NY 12222, USA

(PM) and ozone at ground level near surface are the critical parameters to issue warning or alert to the public. Ground level or “bad” ozone is not emitted directly into the air, but is created by chemical reactions between oxides of nitrogen ( $\text{NO}_x$ ) and volatile organic compounds (VOC) in the presence of sunlight (Seinfeld and Pandis 2006). The ozone can also be formed during biomass burning (Alvarado et al. 2009). Emissions from industrial facilities and electric utilities, motor vehicle exhaust, gasoline vapors, and chemical solvents are some of the major sources of  $\text{NO}_x$  and VOC. Breathing ozone can trigger a variety of health problems, particularly for children, the elderly, and people of all ages who have lung diseases such as asthma. Ground-level ozone can also have harmful effects on sensitive vegetation and ecosystems.

Aerosol sources and gaseous emission are the most important information to the air transport model. The NOAA National Air Quality Forecasting Capability (NAQFC), developed by the NOAA Air Resources Laboratory (ARL) and operated by the National Weather Service (NWS), disseminates NOAA’s real-time model forecasts and satellite observations of air quality to state and local air quality and public health agencies, as well as the general public. The NWS uses the NAQFS to provide air quality warnings and alerts for large cities in the United States. Air quality and public health managers use these forecasts to inform short-term management decisions and longer term policies to reduce the adverse effects of air pollution on human health and their associated economic costs. The NAQFC operational  $\text{O}_3$  and developmental  $\text{PM}_{2.5}$  forecasts consist of three model components: the ARL Emission Forecasting System (EFS), the NWS North American Mesoscale (NAM) regional nonhydrostatic meteorological model, and the modified CMAQ model. They all use 12 km horizontal grid spacing and are coupled in a sequential and offline manner with hourly data fed from NAM to Community Multi-scale Air Quality (CMAQ) hourly. While the “operational”  $\text{O}_3$  forecasts are guaranteed to be available and be disseminated on time to the general public both graphically and in formatted files following World Meteorological Organization (WMO) standards, the dissemination of the “developmental”  $\text{PM}_{2.5}$  forecasts are currently restricted to a selected group of local and state air quality forecasters, the so-called Focus Group Forecasters (FGF) of the NAQFC. The NAQFC is one of the major gateways to disseminate NOAA model prediction and satellite observations of air quality to the public (<http://airquality.weather.gov>). The accuracy of NAQFC forecasts depend on EFS, NAM, and CMAQ in about the same magnitude of forcing. NAM is quite advanced in utilizing satellite data to nudge weather forecast through its data assimilation schemes (Lee and Liu 2014). However, until recently NAQFC has not assimilated the atmospheric composition data from satellite retrievals to improve its emission, transport, and chemical transformation estimates.

Aerosols can affect the energy balance of Earth’s atmosphere through the absorption and scattering of solar and thermal radiation. Aerosols also affect Earth’s climate through their effects on cloud microphysics, reflectance, and precipitation. In

addition, aerosols can be viewed as air pollutants because of their adverse health effects. In NOAA NCEP global forecast system (GFS), the representations of aerosols need to better account for these effects. The aerosol distributions in the forecast model are currently prescribed based on a global climatological aerosol database (Hess et al. 1998) and only the aerosol direct effect is considered. The current data assimilation system assumes climatological aerosol conditions. For atmospheric conditions with anomalous high aerosol loading, bias correction and quality control procedures can be compromised due to the unaccounted effects of aerosol attenuation.

An online aerosol modeling capability in Goddard Chemistry Aerosol Radiation and Transport (GOCART) has been developed and implemented within GMAO's GEOS-5 Earth system model (Colarco et al. 2010) and was later coupled with NCEP's NEMS version of GFS to establish the first interactive atmospheric aerosol forecasting system at NCEP, NGAC (Lu et al. 2013). While the ultimate goal at NCEP is a full-up Earth system with the inclusion of aerosol-radiation feedback and aerosol-cloud interaction, the current operational configuration (as in September 2014) is to maintain a dual-resolution configuration with low-resolution (T126 L64) forecast-only system for aerosol prediction (using NGAC) and a high-resolution (T574 L64) forecasting and analysis system for medium-range weather prediction (using GFS). Aerosol fields in NGAC initial conditions are taken from prior NGAC forecast and the corresponding meteorological fields are downscaled from GFS analysis.

The current dual-resolution system mentioned above feeds meteorological fields from GFS to NGAC. In our study, we will upgrade the infrastructure in the dual-resolution system, allowing NGAC aerosol fields fed into GFS. The linkage between NGAC and GFS to be considered include: using NGAC aerosols fields instead of the climatology (Hess et al. 1998) to determine aerosol optical properties in GFS radiation, enabling the GFS data assimilation system to consider NGAC aerosol fields instead of background aerosol loading for satellite radiances calculations, and incorporating NGAC aerosols fields in sea surface temperature (SST) analysis. Standard forecast verification system will be used to determine whether the improved treatment of aerosols will lead to improvement in weather forecasts. Data rejection will be examined to assess whether improved aerosol treatment will lead to better use of satellite data. Diagnosis of energy budget will be conducted to evaluate whether more realistic temporal and spatial representation of aerosols will result in improved energy balance.

Global ammonia ( $\text{NH}_3$ ) emissions have been increasing due to the dramatically increased agricultural livestock numbers together with the increasing use of nitrogen fertilization (Sutton et al. 2014). Atmospheric ammonia has impacts on local scales, acidification and hypertrophication of the ecosystems, and international scales through formation of fine ammonium-containing aerosols. These ammonium aerosols affect Earth's radiative balance and public health. Measurements with daily and large global coverage are challenging and have been lacking partly because the lifetime of  $\text{NH}_3$  is relatively short (hours to a day) and partly because it requires high sensitivity for the retrievals. The Cross-Track Infrared Sounder (CrIS) and Infrared Atmospheric Sounding Interferometer (IASI) hyperspectral measurements are good for monitoring  $\text{NH}_3$  emissions due to their large daily global coverage and

afternoon overpasses that provide higher thermal contrasts, and hence, higher measurement sensitivities.

NH<sub>3</sub> contributes to the formation of PM<sub>2.5</sub> by reaction with nitric and sulfuric acids (HNO<sub>3</sub> and H<sub>2</sub>SO<sub>4</sub>), which are in turn formed by the photochemical oxidation of nitrogen oxides (NO<sub>x</sub> = NO + NO<sub>2</sub>) and sulfur dioxide (SO<sub>2</sub>), respectively. In the United States, it is estimated that livestock accounts for about 74 % of total anthropogenic NH<sub>3</sub> emissions, with an additional 16 % due to the manufacturing and use of fertilizer (Potter et al. 2010), although these estimates are uncertain. Reductions of NH<sub>3</sub> emissions have been proposed as a cost effective way to improve air quality.

As emphasized above, aerosol sources and gaseous emission are very critical information affecting air quality analysis and prediction. Observations from satellites provide information about global aerosol sources and gaseous emission. However, the sensors onboard satellites measure radiation rather than aerosols or trace gases. To derive aerosol and trace gas from the satellite measurements, inversion technique in retrieval algorithm or radiance assimilation are needed where radiative transfer models play an important role to interpret the meaning of the radiation to geophysical parameters. The CRTM is such an operational radiative transfer model for passive microwave, infrared, and visible sensors.

## 2 What Are the Common Air Pollutants?

Pollutants are harmful to public health and the environment. The US Environment Protection Agency (EPA) identified six common air pollutants (<http://www.epa.gov/air/criteria.html>). They are particle (aerosol) pollution (often referred to as particulate matter in the atmosphere), ground-level ozone, carbon monoxide, sulfur oxides, nitrogen oxides, and lead. These pollutants can harm public health and the environment, and cause property damage. Of the six pollutants, particle pollution and ground-level ozone are the most widespread health threats. The first real-time product of NAQFC is ozone. Recently, NAQFC starts to provide PM<sub>2.5</sub> (i.e., particulate matter size less than 2.5 μm in diameter) forecasts to early adapter users (“the focus group”), predominantly state environmental agencies that use NAQFC daily products for numeric air quality guidance. EPA calls these pollutants “criteria” air pollutants because it regulates them by developing human health-based and/or environmentally based criteria (science-based guidelines) for setting permissible levels. The set of limits based on human health is called primary standards. Another set of limits intended to prevent environmental and property damage is called secondary standards.

EPA has set National Ambient Air Quality Standards for six principal pollutants (<http://www.epa.gov/air/criteria.html>), which are called “criteria” pollutants. They are listed below. Units of measure for the standards are parts per million (ppm) by volume, parts per billion (ppb) by volume, and micrograms per cubic meter of air (μg m<sup>-3</sup>) (see Table 1).

**Table 1** Six principal pollutants identified by US Environmental Protection Agency

Pollutant [final rule cite]	Primary/secondary	Averaging Time	Level	Form
Carbon monoxide [76 FR 54294, Aug 31, 2011]	Primary	8-h	9 ppm	Not to be exceeded more than once per year
		1-h	35 ppm	
Lead [73 FR 66964, Nov 12, 2008]	Primary and secondary	Rolling 3 month average	0.15 µg/m <sup>3</sup> <sub>a</sub>	Not to be exceeded
Nitrogen dioxide [75 FR 6474, Feb 9, 2010] [61 FR 52852, Oct 8, 1996]	Primary	1-h	100 ppb	98th percentile of 1-h daily maximum concentrations, averaged over 3 years
	Primary and secondary	Annual	53 ppb <sup>b</sup>	Annual mean
Ozone [73 FR 16436, Mar 27, 2006]	Primary and secondary	8-h	0.075 ppm <sup>c</sup>	Annual fourth highest daily maximum 8-h concentration, averaged over 3 years
Particle pollution Dec 14, 2012	Primary	Annual	12 µg/m <sup>3</sup>	Annual mean, averaged over 3 years
	Secondary	Annual	15 µg/m <sup>3</sup>	Annual mean, averaged over 3 years
	Primary and secondary	24-h	35 µg/m <sup>3</sup>	98th percentile, averaged over 3 years
Sulfur dioxide [75 FR 35520, Jun 22, 2010] [38 FR 25678, Sept 14, 1973]	Primary and secondary	24-h	150 µg/m <sup>3</sup>	Not to be exceeded more than once per year on average over 3 years
	Primary	1-h	75 ppb <sup>d</sup>	99th percentile of 1-h daily maximum concentrations, averaged over 3 years
	Secondary	3-h	0.5 ppm	Not to be exceeded more than once per year

Detailed description of the following tables is referred to the EPA website (<http://www.epa.gov/ttn/naaqs/criteria.html>)

<sup>a</sup>Previous standards; current (2008) standards have not been submitted and approved

<sup>b</sup>The level of the annual NO<sub>2</sub> standard

<sup>c</sup>The previous (2008) O<sub>3</sub> standards additionally remain in effect in some areas

<sup>d</sup>The previous SO<sub>2</sub> standards (0.14 ppm 24-hour and 0.03 ppm annual) will additionally remain in effect in certain areas

## **2.1 Air Pollutants**

### **2.1.1 Ozone**

Ozone in the stratosphere is good to protect human from harmful ultraviolet radiation. Oxygen, nitrogen, and ozone block more than 95 % UV radiation from Sun to the Earth's surface. UV light may be divided into three bands: UVC [100–280 nm], UVB (280–315 nm), and UVA (315–400 nm). UVC is the most dangerous, but it is mostly absorbed by oxygen and ozone molecules in the stratosphere and does not reach the Earth's surface. The sun's UV radiation is both a major cause of skin cancer and the best natural source of vitamin D. Therefore, we need a proper UV exposure. Clouds are often opaque that blocks sun's radiation. But, broken clouds may scatter more sun's radiation including UV component due to the three-dimensional radiative transfer. Ozone in the stratosphere is good. The ground-level ozone is bad for public health. Ground-level ozone is not emitted directly into the air, but is created by chemical reactions between oxides of nitrogen ( $\text{NO}_x$ ) and volatile organic compounds (VOC) in the presence of sunlight. Emissions from industrial facilities and electric utilities, motor vehicle exhaust, gasoline vapors, and chemical solvents are some of the major sources of  $\text{NO}_x$  and VOC. Breathing ozone can trigger a variety of health problems, particularly for children, the elderly, and people of all ages who have lung diseases such as asthma. Ground-level ozone can also have harmful effects on sensitive vegetation and ecosystems.

### **2.1.2 Particulate Matter**

Particulate matter or suspended matter in the atmosphere also known as particle pollution or PM, is a complex mixture of small particles and liquid droplets. Particle pollution is made up of a number of components, including nitrates, sulfates, ammonium, organic chemicals, metals, and soil or dust particles (<http://www.epa.gov/airquality/particlepollution/>). In the cities, fine particles primarily come from car, truck, bus, and off-road vehicle exhausts, other operations involve biomass burning, heating oil or coal and natural sources. Fine particles also form from the reaction of gases or droplets in the atmosphere from sources such as power plants. The size of particles is directly linked to their potential for causing health problems. EPA is concerned about particles that are 10  $\mu\text{m}$  in diameter or smaller because those are the particles that generally pass through the throat and nose and enter the lungs. Once inhaled, these particles can affect the heart and lungs and cause serious health effects. EPA groups particle pollution into two categories:

- “Inhalable coarse particles,” such as those found near roadways and dusty industries, are larger than 2.5  $\mu\text{m}$  and smaller than 10  $\mu\text{m}$  in diameter. Particles less than 10  $\mu\text{m}$  in diameter ( $\text{PM}_{10}$ ) pose a health concern because they can be inhaled into and accumulate in the respiratory system.

- “Fine particles,” such as those found in smoke and haze, are  $2.5\text{ }\mu\text{m}$  in diameter and smaller. These particles can be directly emitted from sources such as forest fires, or they can form when gases emitted from power plants, industries, and automobiles react in the air. Particles less than  $2.5\text{ }\mu\text{m}$  in diameter ( $\text{PM}_{2.5}$ ) are referred to as “fine” particles and are believed to pose the greatest health risks.

The EPA categorized air quality to six classes based on PM concentrations <http://airnow.gov/index.cfm?action=aqibasics.aqi>):  $0\text{--}50\text{ }\mu\text{g m}^{-3}$  (excellent),  $50\text{--}100\text{ }\mu\text{g m}^{-3}$  (good),  $100\text{--}150\text{ }\mu\text{g m}^{-3}$  (lightly polluted),  $150\text{--}200\text{ }\mu\text{g m}^{-3}$  (moderately polluted),  $200\text{--}300\text{ }\mu\text{g m}^{-3}$  (heavily polluted),  $300\text{--}500\text{ }\mu\text{g m}^{-3}$  (severely polluted), and  $>500\text{ }\mu\text{g m}^{-3}$  (hazardous). Weather conditions and topography can play an important role in local air quality. Outdoor  $\text{PM}_{2.5}$  levels are most likely to be elevated on days with little or no wind or air mixing.  $\text{PM}_{2.5}$  can also be produced by common indoor activities. Some indoor sources of fine particles are tobacco smoke, cooking (e.g., frying, sautéing, and broiling), burning candles or oil lamps, and operating fireplaces and fuel-burning space heaters (e.g., kerosene heaters). One may acquire  $\text{PM}_{2.5}$  at nearly real-time online, for example, the air quality in Beijing may be obtained from the website <http://aqicn.org/city/beijing/>.

### 2.1.3 Carbon Monoxide

Carbon monoxide (CO) is a colorless, odorless gas emitted from incomplete combustion processes. In urban areas, the majority of CO emissions to ambient air come from mobile sources. In rural areas, biomass burning and forest fires release tremendous CO. CO can cause harmful health effects by reducing oxygen delivery to the body’s organs (like the heart and brain) and tissues. At extremely high levels, CO can cause death.

### 2.1.4 Nitrogen Oxides

Nitrogen dioxide ( $\text{NO}_2$ ) is one of a group of highly reactive gases known as “oxides of nitrogen,” or “nitrogen oxides ( $\text{NO}_x$ ).” Other nitrogen oxides include nitrous acid and nitric acid. EPA’s National Ambient Air Quality Standard uses  $\text{NO}_2$  as the indicator for the larger group of nitrogen oxides.  $\text{NO}_2$  forms quickly from emissions from cars, trucks and buses, power plants, and off-road equipment. In addition to contributing to the formation of ground-level ozone, and fine particle pollution,  $\text{NO}_2$  is linked with a number of adverse effects on the respiratory system.

EPA first set standards for  $\text{NO}_2$  in 1971, setting both a primary standard (to protect health) and a secondary standard (to protect the public welfare) at 53 parts per billion (ppb), averaged annually. The Agency has reviewed the standards twice since that time, but chose not to revise the annual standards at the conclusion of each review. In January 2010, EPA established an additional primary standard at 100 ppb, averaged over one hour. Together the primary standards protect public

health, including the health of sensitive populations—people with asthma, children, and the elderly. No area of the country has been found to be out of compliance with the current NO<sub>2</sub> standards.

### **2.1.5 Sulfur Dioxide**

Sulfur dioxide (SO<sub>2</sub>) is one of a group of highly reactive gases known as “oxides of sulfur.” The largest sources of SO<sub>2</sub> emissions are from fossil fuel combustion at power plants (73 %) and other industrial facilities (20 %) as well as Volcanic emissions. Smaller sources of SO<sub>2</sub> emissions include industrial processes such as extracting metal from ore, and the burning of high sulfur-containing fuels by locomotives, large ships, and non-road equipments. SO<sub>2</sub> is linked with a number of adverse effects on the respiratory system.

EPA first set standards for SO<sub>2</sub> in 1971. EPA set a 24-h primary standard at 140 ppb and an annual average standard at 30 ppb (to protect health). EPA also set a 3-h average secondary standard at 500 ppb (to protect the public welfare). In 1996, EPA reviewed the SO<sub>2</sub> NAAQS and chose not to revise the standards.

### **2.1.6 Lead**

Lead is a metal found naturally in the environment as well as in manufactured products. The major sources of lead emissions have historically been from fuels in on-road motor vehicles (such as cars and trucks) and industrial sources. Old painting before 1978 can contain harmful lead. As a result of EPA’s regulatory efforts to remove lead from on-road motor vehicle gasoline, emissions of lead from the transportation sector dramatically declined by 95 % between 1980 and 1999, and levels of lead in the air decreased by 94 % between 1980 and 1999. Today, the highest levels of lead in air are usually found near lead smelters. The major sources of lead emissions to the air today are ore and metals processing and piston engine aircraft operating on leaded aviation gasoline.

## **3 Satellite Data for Studying Air Quality**

Satellite remote sensing of air quality has been evolved over last decades. Although the space-borne sensor cannot directly measure the particulate matters or aerosols and trace gases such as CO, NO<sub>2</sub>, O<sub>3</sub>, and SO<sub>2</sub>, we are able to analyze scattered and emitted radiation to accurately derive aerosols and trace gases. The space-borne instruments can be divided into active and passive sensors. The active-sensed instruments, for example, Cloud-Aerosol Lidar and Infrared Pathfinder Satellite Observations (CALIPSO) launched on April 28, 2006, sent out signals and received the backscattered signals. Using the backscattered signals, one may be able to



determine aerosol type and mass concentrations (Liu et al. 2009). Most of space-borne remote sensing sensors are passive, which receive from atmosphere/surface scattered and emitted radiation. The visible channels of POLDER, MODIS (Liang et al. 2006), and VIIRS (Cao et al. 2013) have been successfully used to derive aerosol optical depths over dark surfaces. SeaWiFS was for ocean color products. The data are found very valuable to obtain aerosol optical depth over oceans. The ultraviolet sensors like Global Ozone Monitoring Experiment-2 (GOME-2), ozone monitoring instrument (OMI), and ozone mapping profiler suite (OMPS) (Wu et al. 2014) are sensitive to aerosols in particular to absorbing aerosols, although the primary application of those UV sensors is for ozone retrievals. Many passive sensors have been used to derive the products of chemical compositions in the atmosphere. The Earth Observing System (EOS) Microwave Limb Sounder (MLS) on the NASA's EOS Aura satellite, launched on July 15, 2004, has demonstrated great success in retrieving ozone and other atmospheric compositions. MLS observes thermal microwave emission from Earth's "limb" (the edge of the atmosphere) viewing forward along the Aura spacecraft flight direction, scanning its view from the ground to  $\sim 90$  km every  $\sim 25$  s. The instrument for the Measurements of Pollution in the Troposphere (MOPITT) is a payload scientific instrument launched into Earth orbit by NASA on board the Terra satellite on December 18, 1999. MOPITT's near-infrared radiometer at 2.3 and 4.7  $\mu\text{m}$  specific focus is on the distribution, transport, sources, and sinks of carbon monoxide in the troposphere. Carbon monoxide, which is expelled from factories, cars, and forest fires, hinders the atmosphere's natural ability to rid itself of harmful pollutants.

The Global Ozone Monitoring Experiment-2 (GOME-2), a European instrument flying on the MetOp-A series of satellites (Launched on October 19, 2006) was designed by the European Space Agency to measure atmospheric ozone trace gases and ultraviolet radiation <http://www.eumetsat.int/website/home/Satellites/CurrentSatellites/Metop/MetopDesign/GOME2/index.html>). It is a scanning instrument (scan width 1920 km) with near global coverage daily. The field of view on the ground is 80 km by 40 km. It also provides accurate information on the total column amount of nitrogen dioxide, sulfur dioxide, water vapor, oxygen/oxygen dimmer, bromine oxide, and other trace gases, as well as aerosols.

The Multi-angle Imaging SpectroRadiometer (MISR) is a scientific instrument on the Terra satellite launched by NASA on December 18, 1999. This device is designed to measure the intensity of solar radiation reflected by the Earth system (planetary surface and atmosphere) in various directions and spectral bands; it became operational in February 2000. Data generated by this sensor have been proven useful in a variety of applications including atmospheric sciences, climatology, and monitoring terrestrial processes.

The MISR instrument consists of an innovative configuration of nine separate digital cameras that gather data in four different spectral bands of the solar spectrum. One camera points toward the nadir, while the others provide forward and afterward view angles at  $26.1^\circ$ ,  $45.6^\circ$ ,  $60.0^\circ$ , and  $70.5^\circ$ . As the instrument flies

overhead, each region of the Earth's surface is successively imaged by all nine cameras in each of four wavelengths (blue, green, red, and near-infrared).

The data gathered by MISR are useful in climatological studies concerning the disposition of the solar radiation flux in the Earth's system. MISR is specifically designed to monitor the monthly, seasonal, and long-term trends of atmospheric aerosol particle concentrations including those formed by natural sources and by human activities, upper air winds and cloud cover, type, height, as well as the characterization of land surface properties, including the structure of vegetation canopies, the distribution of land cover types, or the properties of snow and ice fields, amongst many other biogeophysical variables.

NESDIS GOME 2 (MetOp-A) total ozone products, based on the SBUV/2 version 8 algorithms are produced in binary and BUFR formats. The algorithm also produces aerosol index and reflectivity values, which are included in the total ozone binary product.

Infrared hyperspectral sensors such as AIRS, IASI, and CrIS are useful to retrieve trace gases. IASI samples radiance in a spectral resolution of  $0.25\text{ cm}^{-1}$ , providing a high sensitivity to trace gases. CrIS data of a full spectral resolution of  $0.625\text{ cm}^{-1}$  can be used to derive CO (Liu and Xiao 2014).

## 4 Community Radiative Model

CRTM is a sensor-based radiative transfer model. It supports more than 100 sensors including sensors on most meteorological satellites and some from other remote sensing satellites. The CRTM is composed of four important modules for gaseous transmittance, surface emission and reflection, cloud and aerosol absorption and scatterings, and a solver for a radiative transfer. The CRTM was designed to meet users' needs. Many options are available for users to choose: input surface emissivity; select a subset of channels for a given sensor; turn off scattering calculations; compute radiance at aircraft altitudes; compute aerosol optical depth only; and threading of the CRTM. Figure 1 shows the interface diagram for users (public interface) and internal modules for developers contained in the lower dashed box. The CRTM forward model is used to simulate from satellite-measured radiance, which can be used to verify measurement accuracy, uncertainty, and long-term stability. The k-matrix module is used to compute jacobian values (i.e., radiance derivative to geophysical parameters), which is used for the inversion processing in retrieval and radiance assimilations. Using tangent linear and adjoint modules is equivalent to using k-matrix module and is also applied to some application in radiance assimilation. In the following subsessions, we will describe the CRTM modules in detail.

The CRTM is a library for users to link, instead of a graphic user interface. By the CRTM initialization, user selects the sensor/sensors and surface emissivity/reflectance lookup tables. Developers may incorporate their own expertise into the CRTM for any desired applications. The gaseous transmittance describes atmospheric gaseous

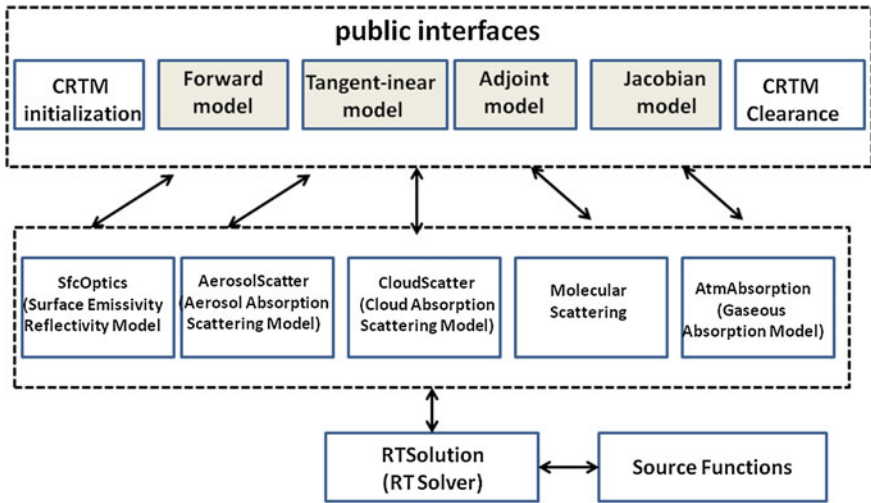


**Fig. 1** An interface diagram of the community radiative transfer model. The modules in the public interfaces (*upper dashed box*) are accessed by users. The modules below the *upper dashed box* are for developers

absorption, so that one can utilize remote sensing information in data assimilation/retrieval systems for atmospheric temperature, moisture, and trace gases such as  $\text{CO}_2$ ,  $\text{O}_3$ ,  $\text{N}_2\text{O}$ ,  $\text{CO}$ , and  $\text{CH}_4$  (Chen et al. 2012). The aerosol module is fundamental to acquire aerosol type and concentration for studying air quality. The cloud module contains optical properties of six cloud types, providing radiative forcing information for weather forecasting and climate studies. The CRTM surface model includes surface static and atlas-based emissivity/reflectivity for various surface types. Two radiative solutions have been implemented into the CRTM. The advanced doubling-adding (ADA) method (Liu and Weng 2013, 2006) is chosen as a baseline. The successive order of interaction (SOI) radiative transfer model (Heidinger et al. 2006) developed at the University of Wisconsin, has also been implemented in the CRTM.

For a new sensor, the CRTM team can generate spectral and transmittance coefficient files as long as the spectral response data of the new sensor is available. Once the spectral and transmittance coefficient files are created, the CRTM is ready for the new sensor. The new surface emissivity model may be supplied if the user wants to derive surface emissivity for the new sensor. The CRTM user interface provides forward, tangent linear, adjoint, and k-matrix functions to compute radiance (also microwave and infrared brightness temperature) and sensitivities of radiance to atmospheric/surface parameters. The NOAA Microwave Integrated Retrieval System (MiRS) (Boukabara et al. 2007) and NCEP data assimilation system use the k-matrix. The Weather and Research Forecasting (WRF) model uses the tangent linear and adjoint models. The NOAA Integrated Calibration/Validation

System Long-term monitoring system (<http://www.star.nesdis.noaa.gov/icvs/>) uses the forward model to compare the CRTM simulation with satellite measurements.

The validation of radiative transfer calculations is very challenging because it depends on the model assumptions (e.g., spherical or nonspherical scatterers), measurement errors, uncertainties in inputs, and others. Many evaluations of the CRTM model simulations versus observations have been performed. Saunder et al. (Saunders et al. 2007) summarized the brightness temperature differences between the line-by-line (LBL) model and fast radiative transfer models including the CRTM where the Optical Path Transmittance (OPTRAN) algorithm is used. The difference in the standard deviation under clear-sky conditions is generally less than 0.1 K for the Atmospheric Infrared Sounder (AIRS). Under cloudy conditions, the difference for the AIRS is about 0.2 K (Ding et al. 2011). Due to the approximation in cloud scattering calculations, the difference between the LBL model and the CRTM for the High-Resolution Infrared Radiation Sounder/3 (HIRS/3) under cloudy conditions can reach 0.4 K (Liu et al. 2013). It is more difficult to estimate the errors between the CRTM model calculations and measurements. We can only give the estimate from limited applications. Liang et al. (2009) implemented the CRTM into the NOAA Monitoring System of IR Clear-sky Radiances over Oceans. The difference between the CRTM simulations and NOAA *Advanced Very High Resolution Radiometer* (AVHRR) observations is about 0.5 K. For the Stratosphere Sounding Unit (SSU), the difference is about 1 K (Liu and Weng 2009). Han et al. (2007) compared the CRTM simulations with the *Special Sensor Microwave Imager/Sounder* (SSMIS) measurements and found both agreed within about 2 K. NOAA NCEP (<http://www.emc.ncep.noaa.gov/gmb/gdas/radiance/esafford/wopr/index.html>) monitors the difference under clear-sky conditions for more than 20 sensors and found that the difference is generally less than 1 K. Under cloudy conditions, uncertainties in inputs are the main source, resulting in a large difference. The difference is about 2 K for microwave sounding channels and 4 K for microwave window channels (Chen et al. 2008).

#### 4.1 Radiative Transfer Equation and Solver

The CRTM is one-dimensional radiative transfer model. This implies that atmosphere is assumed homogeneous in the horizontal direction, so-called a plane-parallel atmosphere. For the plane-parallel atmosphere, a vector radiative transfer model can be written as

$$\mu \frac{d\mathbf{I}(\tau, \Omega)}{d\tau} = -\mathbf{I}(\tau, \Omega) + \frac{\varpi}{4\pi} \int_0^{2\pi} \int_{-1}^1 \mathbf{M}(\tau; \Omega; \Omega') \mathbf{I}(\tau, \Omega') d\Omega' + \mathbf{S}(\tau, \Omega; \Omega_0), \quad (1a)$$

where  $\Omega$  represents a beam for a pair  $(\mu, \phi)$  in an incoming or an outgoing direction or

$$\mu \frac{d\mathbf{I}(\tau, \mu, \phi)}{d\tau} = -\mathbf{I}(\tau, \mu, \phi) + \frac{\varpi}{4\pi} \int_0^{2\pi} \int_{-1}^1 \mathbf{M}(\tau; \mu, \phi; \mu', \phi') \mathbf{I}(\tau, \mu', \phi') d\mu' d\phi' + \mathbf{S}(\tau, \mu, \phi; \mu_0, \phi_0) \quad (1b)$$

and

$$\mathbf{S} = (1 - \varpi) B[T(\tau)] \begin{bmatrix} 1 \\ 0 \\ 0 \\ 0 \end{bmatrix} + \frac{\varpi F_0}{4\pi} \exp(-\tau/\mu_0) \begin{bmatrix} M_{11}(\mu, \phi; \mu_0, \phi_0) \\ M_{12}(\mu, \phi; \mu_0, \phi_0) \\ M_{13}(\mu, \phi; \mu_0, \phi_0) \\ M_{14}(\mu, \phi; \mu_0, \phi_0) \end{bmatrix}, \quad (1c)$$

where  $\mathbf{M}$  is the phase matrix;  $\mathbf{I} = [I, Q, U, V]^T$ ;  $B(T)$  the Planck function at a temperature  $T$ ;  $F_0$  the solar spectral constant;  $\mu_0$  the cosine of sun zenith angle;  $\varpi$  the single-scattering albedo; and  $\tau$  the optical thickness.

Equation (1a) can be solved by a standard discrete method for beams rather than separate zenith angles from azimuthal angles. The advantage of this approach is that one can directly use the phase function without doing any truncation. The disadvantage is that it demands more memory for a large number of beams that can slow the computation. The approach can be useful for more accurate simulations in the future when computational capacity increases.

Equation (1b) is commonly used in radiative transfer models including the CRTM. The equation can be solved by some standard routines such as the multi-layer discrete ordinate method (Stamnes et al. 1988), the Doubling-adding method (Evans and Stephens 1991), and the matrix operator method (Liu and Ruprecht 1996). Essentially, the azimuthal dependence of Stokes vector is expanded into a series of Fourier harmonics. The amplitude of each Fourier component is a function of zenith angles. Furthermore, the amplitude is discretized at a series of zenith angles (or streams) so that the combined Stokes cosine and sine harmonics can be simplified as

$$\begin{aligned} \mu_i \frac{d}{d\tau} \begin{bmatrix} \mathbf{I}_m(\tau, \mu_i) \\ -\mathbf{I}_m(\tau, \mu_{-i}) \end{bmatrix} &= \begin{bmatrix} \mathbf{I}_m(\tau, \mu_i) \\ \mathbf{I}_m(\tau, \mu_{-i}) \end{bmatrix} \\ &- \varpi \sum_{j=1}^N \begin{bmatrix} \mathbf{M}_m(\mu_i, \mu_j) & \mathbf{M}_m(\mu_i, \mu_{-j}) \\ \mathbf{M}_m(\mu_{-i}, \mu_j) & \mathbf{M}_m(\mu_{-i}, \mu_{-j}) \end{bmatrix} \begin{bmatrix} \mathbf{I}_m(\tau, \mu_j) \\ \mathbf{I}_m(\tau, \mu_{-j}) \end{bmatrix} w_j \\ &- \begin{bmatrix} \mathbf{S}_m(\tau, \mu_i, \mu_0) \\ \mathbf{S}_m(\tau, \mu_{-i}, \mu_0) \end{bmatrix}. \end{aligned} \quad (2)$$

where  $\mu_i$  and  $w_i$  are Gaussian quadrature points and weights, respectively. Note that  $\mu_{-i} = -\mu_i$  and  $w_{-i} = w_i$ . According to the properties of the phase matrix, the radiance components at sinusoidal and cosinusoidal modes can be decoupled, recombined, and solved independently (Weng and Liu 2003).

The summation in Eq. (2) is over discrete zenith angles or streams. For  $N = 1$  in Eq. (2), it is called two-stream radiative transfer to represent one upward and one downward directions. It is called eight-stream radiative transfer when  $N = 4$ . The computational time is proportional to  $N^3$ .

In most radiative transfer schemes, the phase function can be expanded in terms of Legendre polynomials as follows:

$$P(\cos \Theta) = \sum_{l=0}^M \omega_l P_l(\cos \Theta) \quad (3)$$

where  $\Theta$  is the scattering angle,  $P_l(\cos \Theta)$  are Legendre polynomials,  $\omega_l$  are the expansion coefficients, and the value of the upper summation limit  $M$  should be equal or smaller than  $N$  used in Eq. (2).

Thousands of terms may be required for accurate phase function of an ice cloud in the visible spectrum, but the computation burden makes this an unattractive approach. One way of reducing the necessary Legendre terms is by truncating the forward scattering peak and renormalizing the phase function. Wiscombe (1957) proposed a  $\delta$ - $M$  method to truncate Legendre polynomials. The  $\delta$ - $M$  method can effectively remove the forward peak in a rigorous mathematical way, but it may cause large spikes in the phase function for small scattering angles ( $< 20^\circ$ ). The  $\delta$ -fit method (Hu et al. 2000) truncates the forward scattering peak in the phase function and more optimally fits the remaining phase function by selecting a set of optimized expansion coefficients in Eq. (3). We applied the  $\delta$ -fit method in this study.

To achieve the same accuracy in multiple scattering calculations with the truncated phase functions as with the nontruncated phase functions, an adjustment must be made to the optical thickness and single-scattering albedo via the following relations (Liou 2002):

$$\tau' = (1 - f\omega)\tau, \quad (4)$$

$$\omega' = \frac{(1 - f)\omega}{1 - f\omega}, \quad (5)$$

where  $f$  indicates the portion of the scattered energy associated with the truncated forward peak. In Eqs. (4) and (5),  $\tau$  and  $\omega$  are the original optical thickness and single-scattering albedo, respectively, whereas  $\tau'$  and  $\omega'$  are the optical thickness and single-scattering albedo associated with the truncated phase function.

After we have the phase matrix, Eq. (2) for each harmonic component can be expressed as

$$\frac{d\mathbf{I}}{d\tau} = \mathbf{A}\mathbf{I} - \mathbf{S}, \quad (6)$$

where

$$\mathbf{I} = [\mathbf{I}(\tau, \mu_1), \mathbf{I}(\tau, \mu_2), \dots, \mathbf{I}(\tau, \mu_N), \mathbf{I}(\tau, \mu_{-1}), \mathbf{I}(\tau, \mu_{-2}), \dots, \mathbf{I}(\tau, \mu_{-N})]^T, \quad (7)$$

$$\mathbf{S} = (1 - \varpi)B(T)\delta_{m0} \begin{bmatrix} \mathbf{u}^{-1} & \mathbf{0} \\ \mathbf{0} & -\mathbf{u}^{-1} \end{bmatrix} \Xi + \frac{\varpi F_0}{\pi} \exp(-\tau/\mu_0) \Psi, \quad (8)$$

where  $\mathbf{u}$  is a  $4N$  by  $4N$  matrix that has nonzero elements at its diagonal direction such as

$$u = [\mu_1, \mu_1, \mu_1, \mu_1, \mu_2, \dots, \mu_N, \mu_N, \mu_N, \mu_N]_{\text{diagonal}}, \quad (9a)$$

$\Xi$  and  $\Psi$  are vectors that have  $8N$  elements as

$$\Xi = [1, 0, 0, 0, 1, 0, 0, 0, \dots, 1, 0, 0, 0]^T; \quad (9b)$$

and

$$\begin{aligned} \Psi = & [M_{11}(\mu_1, \mu_0)/\mu_1, M_{12}(\mu_1, \mu_0)/\mu_1, M_{13}(\mu_1, \mu_0)/\mu_1, M_{14}(\mu_1, \mu_0)/\mu_1, \\ & M_{11}(\mu_2, \mu_0)/\mu_2, M_{12}(\mu_2, \mu_0)/\mu_2, M_{13}(\mu_2, \mu_0)/\mu_2, M_{14}(\mu_2, \mu_0)/\mu_2, \dots, \\ & M_{11}(\mu_{-N}, \mu_0)/\mu_{-N}, M_{12}(\mu_{-N}, \mu_0)/\mu_{-N}, M_{13}(\mu_{-N}, \mu_0)/\mu_{-N}, M_{14}(\mu_{-N}, \mu_0)/\mu_{-N}], \end{aligned} \quad (9c)$$

and the composite phase matrix

$$\mathbf{A} = \begin{bmatrix} \mathbf{u}^{-1} & \mathbf{0} \\ \mathbf{0} & -\mathbf{u}^{-1} \end{bmatrix} \begin{bmatrix} \mathbf{E} - \varpi \mathbf{M}(u, u) & \varpi \mathbf{M}(u, -u) \\ \varpi \mathbf{M}(-u, u) & \mathbf{E} - \varpi \mathbf{M}(-u, -u) \end{bmatrix} = \begin{bmatrix} \boldsymbol{\alpha}_1 & \boldsymbol{\beta}_1 \\ -\boldsymbol{\beta}_2 & -\boldsymbol{\alpha}_2 \end{bmatrix} \quad (9d)$$

where  $\mathbf{E}$  is a unit matrix. For a pair of zenith angles  $(\mu_i, \mu_j)$ , both  $\boldsymbol{\alpha}$  and  $\boldsymbol{\beta}$  are  $4N$  by  $4N$  matrices and are related to the elements of the phase matrices as

$$\boldsymbol{\alpha}_1(\mu_i, \mu_j) = [\mathbf{E} - \varpi \mathbf{M}_m(\mu_i, \mu_j)]/\mu_i \quad (10a)$$

$$\boldsymbol{\beta}_1(\mu_i, \mu_{-j}) = \varpi \mathbf{M}_m(\mu_i, \mu_{-j})/\mu_i \quad (10b)$$

$$\boldsymbol{\alpha}_2(\mu_{-i}, \mu_{-j}) = [\mathbf{E} - \varpi \mathbf{M}_m(\mu_{-i}, \mu_{-j})]/\mu_i \quad (10c)$$

$$\boldsymbol{\beta}_2(\mu_{-i}, \mu_j) = \varpi \mathbf{M}_m(\mu_{-i}, \mu_j)/\mu_i \quad (10d)$$

Equations (1b) to (10a–10d) are a common approach needed by radiative solvers. The equations can be solved using double-adding (Evans and Stephens 1991), matrix operator method (MOM) (Liu and Weng 2013; Liu and Ruprecht 1996), VDISORT (Weng and Liu 2003), Successive Order of Interaction (SOI) Radiative Transfer Model (Heidinger et al. 2006), and advanced double-adding (ADA) method. In the following, we discuss the ADA for radiative intensity only, a scalar radiative transfer model. The ADA is a default solver in the CRTM. SOI can be selected by users. Both thermal emission source and solar reflection parts are used operationally in supporting of radiance assimilation and satellite products generations. The thermal emission part was documented in the paper (Liu and Weng 2006). The description of the solar reflection part will be added here. Equation (6) for intensity only can be rewritten in a matrix–vector form as

$$\begin{aligned} \frac{d}{d\tau} \begin{bmatrix} \mathbf{I}_u \\ \mathbf{I}_d \end{bmatrix} = - \begin{bmatrix} \boldsymbol{\alpha} & \boldsymbol{\beta} \\ -\boldsymbol{\beta} & -\boldsymbol{\alpha} \end{bmatrix} \begin{bmatrix} \mathbf{I}_u \\ \mathbf{I}_d \end{bmatrix} - (1 - \varpi)B(T) \begin{bmatrix} \mathbf{u}^{-1}\boldsymbol{\Xi} \\ -\mathbf{u}^{-1}\boldsymbol{\Xi} \end{bmatrix} \\ + \frac{\varpi F_0}{\pi} \exp(-\tau/\mu_0) \begin{bmatrix} \mathbf{u}^{-1}\boldsymbol{\Phi}_u \\ -\mathbf{u}^{-1}\boldsymbol{\Phi}_d \end{bmatrix} \end{aligned} \quad (11)$$

where  $\boldsymbol{\alpha}$  and  $\boldsymbol{\beta}$  are  $N$  by  $N$  matrices (All bold letters and symbols indicate either matrix or vector.) and

$$\boldsymbol{\alpha}(\mu_i, \mu_j) = [\varpi P(\mu_i, \mu_j)w_j - \delta_{ij}]/\mu_i, \quad (12a)$$

$$\boldsymbol{\beta}(\mu_i, \mu_{-j}) = \varpi P(\mu_i, \mu_{-j})w_j/\mu_i, \quad (12b)$$

$\delta_{ij}$  is the Kronecker delta. The subscripts u and d indicate upward and downward directions, respectively.  $\mathbf{u}$  is an  $N$  by  $N$  matrix that has nonzero elements in its diagonal such as

$$\mathbf{u} = [\mu_1, \mu_2, \dots, \mu_N]_{\text{diagonal}}, \quad (12c)$$

$\boldsymbol{\Xi}$  is a vector of  $N$  elements as

$$\boldsymbol{\Xi} = [1, 1, \dots, 1]^T. \quad (12d)$$

For an infinitesimal optical depth  $\delta_0$ , multiple scattering can be neglected and the reflection matrix can be expressed as (Plass et al. 1973)

$$\mathbf{r}(\delta_0) = \delta_0 \boldsymbol{\beta}, \quad (12e)$$

and the transmission matrix can be written as

$$\mathbf{t}(\delta_0) = \mathbf{E} + \boldsymbol{\alpha}\delta_0, \quad (12f)$$

$\mathbf{E}$  is an  $N$  by  $N$  unit matrix.



Using the doubling procedure from Van de Hulst (1963), the reflection and transmission matrices for a finite optical depth ( $\delta = \delta_n = 2^n \delta_0$ ) can be computed by doubling the optical depth (i.e.,  $\delta_{i+1}/\delta_i = 2$ ) recursively:

$$\mathbf{r}(\delta_{i+1}) = \mathbf{t}(\delta_i)[\mathbf{E} - \mathbf{r}(\delta_i)\mathbf{r}(\delta_i)]^{-1}\mathbf{r}(\delta_i)\mathbf{t}(\delta_i) + \mathbf{r}(\delta_i) \quad (13a)$$

and

$$\mathbf{t}(\delta_{i+1}) = \mathbf{t}(\delta_i)[\mathbf{E} - \mathbf{r}(\delta_i)\mathbf{r}(\delta_i)]^{-1}\mathbf{t}(\delta_i) \quad (13b)$$

for  $i = 0, n - 1$ . We denote  $\mathbf{r}(k) = \mathbf{r}(\delta_n)$  and  $\mathbf{t}(k) = \mathbf{t}(\delta_n)$  for the reflection and transmission matrices of  $k$ th layer.

There exist formulas for building the layer source functions (Heidinger et al. 2006) depending on the Planck function of the temperature at the top of the layer and the gradient of Planck function over the layer optical depth. However, the formulas are complicated and computationally expensive. In this study, we found a very simple and strict expression for the layer source function using the existing layer reflection and transmission matrices. For an atmospheric layer of an optical depth  $\delta$  and having the top temperature of  $T_1$  and the bottom temperature of  $T_2$ , the upward layer source function can be derived as (see Appendix A of (Liu and Weng 2006))

$$\begin{aligned} \mathbf{S}_u = & [(\mathbf{E} - \mathbf{t} - \mathbf{r})B(T_1) - (B(T_2) - B(T_1))\mathbf{t} + \frac{B(T_2) - B(T_1)}{(1 - \varpi g)\delta}(\mathbf{E} + \mathbf{r} - \mathbf{t})\mathbf{u}]\Xi \\ & + \frac{\omega F_0}{\pi} \exp\left(-\frac{\tau}{\mu_0}\right) [(\mathbf{E} - \mathbf{t} \exp\left(-\frac{\delta}{\mu_0}\right))\Psi_u - \mathbf{r}\Psi_d] \end{aligned} \quad (14a)$$

and the downward source of the layer can be written as

$$\begin{aligned} \mathbf{S}_d = & [(\mathbf{E} - \mathbf{t} - \mathbf{r})B(T_1) + (B(T_2) - B(T_1))(\mathbf{E} - \mathbf{r}) + \frac{B(T_2) - B(T_1)}{(1 - \varpi g)\delta}(\mathbf{t} - \mathbf{E} - \mathbf{r})\mathbf{u}]\Xi \\ & + \frac{\omega F_0}{\pi} \exp\left(-\frac{\tau}{\mu_0}\right) \left[ \left( \exp\left(-\frac{\delta}{\mu_0}\right) \mathbf{E} - \mathbf{t} \right) \Psi_d - \mathbf{r} \exp\left(-\frac{\delta}{\mu_0}\right) \Psi_u \right], \end{aligned} \quad (14b)$$

where  $\varpi$  and  $g$  are single-scattering albedo and asymmetry factor of the layer, respectively.  $\tau$  is the optical depth from the top of the atmosphere to the top of this current layer.

$$\begin{bmatrix} \Psi_u \\ \Psi_d \end{bmatrix} = -\frac{\omega F_0}{(1 + \delta_{0m})} \begin{bmatrix} \alpha + \mathbf{E}/\mu_0 & \beta \\ -\beta & \alpha - \mathbf{E}/\mu_0 \end{bmatrix} \begin{bmatrix} \Phi_u \\ \Phi_d \end{bmatrix} \quad (15)$$

The new expressions for the layer source functions take a very little extra computation time. The expression can also be applied for other radiative transfer models such as matrix operator method (Fischer and Grassl 1984).

Equations (13a, 13b)–(14a, 14b) give the layer reflection and transmission matrices as well as the source vectors at the upward and downward directions. For planetary atmosphere, the atmosphere may be divided into  $n$  optically homogeneous layers. The optical properties (e.g., extinction coefficient, single-scattering albedo, and phase matrix) are the same within each layer although the temperature may vary within the layer. The adding method is for integrating the surface and multiple atmospheric layers. The method was applied to flux calculation using a two-stream approximation. The method was also used in radiance calculations with multiple scatterings using a two-stream approximation (Schmetz and Raschke 1981). In the following, we briefly describe the methodology. We denote  $\mathbf{R}_u(k)$  for reflection matrix and  $\mathbf{I}_u(k)$  for radiance vector at the level  $k$  in the upward direction and  $k = n$  and  $k = 0$  represent the surface level and the top of the atmosphere, respectively. The adding method starts from surface without atmosphere. At the surface,  $\mathbf{R}_u(n)$  is the surface reflection matrix and  $\mathbf{I}_u(n)$  equals the surface emissivity vector multiplied by the Planck function at the surface temperature. The upward reflection matrix and radiance at the new level can be obtained by adding one layer from the present level:

$$\mathbf{R}(k-1) = \mathbf{r}(k) + \mathbf{t}(k) [\mathbf{E} - \mathbf{R}(k) \mathbf{r}(k)]^{-1} \mathbf{R}(k) \mathbf{t}(k), \quad (16a)$$

$$\begin{aligned} \mathbf{I}_u(k-1) &= \mathbf{S}_u(k) + \mathbf{t}(k) [\mathbf{E} - \mathbf{R}(k) \mathbf{r}(k)]^{-1} \mathbf{R}(k) \mathbf{S}_d(k) + \mathbf{t}(k) [\mathbf{E} - \mathbf{R}(k) \mathbf{r}(k)]^{-1} \mathbf{I}_u(k) \\ &= \mathbf{S}_u(k) + \mathbf{t}(k) [\mathbf{E} - \mathbf{R}(k) \mathbf{r}(k)]^{-1} [\mathbf{R}(k) \mathbf{S}_d(k) + \mathbf{I}_u(k)]. \end{aligned} \quad (16b)$$

The physical meaning of Eq. (16a, 16b) is obvious. The first term on the right side of Eq. (16a) is the reflectance of the layer to be added. The second term on the right side of Eq. (16a) is the reflectance due to the radiation from the new level transmitted to and multiple reflected by the present level and then transmitted back to the new level. The three terms on the right side of Eq. (16b) represent the upward layer source, from the present level reflected layer downward source, and from the present level transmitted upward radiance, respectively. The upward radiance  $\mathbf{I}_u$  at the top of the atmosphere can be obtained by looping the index from  $k = n$  to  $k = 1$  and adding the contribution from cosmic background radiance (Planck function at the temperature of 2.7 K) vector  $\mathbf{I}_{\text{sky}}$ , that is,

$$\mathbf{I}_u = \mathbf{I}_u(0) + \mathbf{R}_u(0) \mathbf{I}_{\text{sky}} \quad (17)$$

Equations (12a–12f)–(17) give the necessary and sufficient formulas for advanced doubling-adding method. It needs to be mentioned that the above procedure is for the upward radiance at the top of the atmosphere. It is sufficient for the satellite data assimilation. However, an additional loop from the top to the surface is necessary in order to obtain the vertical profiles of radiances at both upward and downward directions.

For the viewing angle departure from the angles at Gaussian quadrature points, an additional stream as extra Gaussian quadrature point associated with an integration weight of zero may be inserted to have  $N$  quadrature points in total in either

upward or downward direction. For this case, the upward intensity vector will contain the upward solutions at  $N - 1$  quadrature points and at a specified viewing angle. The result by inserting the additional stream is exactly the same as inserting the multiple scattering solutions at  $N - 1$  quadrature points back to the integration equation for the specified viewing angle [see Eqs. (24) and (25) of Stamnes et al. (Chen et al. 2008)]. However, the present procedure avoids using extra codes for the specified viewing angle so that it much simplifies all forward, tangent linear, and adjoint codings.

All rigorous discrete radiative transfer solvers should be very accurate. The model intercomparisons in the paper (Liu and Weng 2006) are adopted here between the doubling-adding model (Evans and Stephens 1991), VDISORT (Weng and Liu 2003), and the advanced doubling-adding method. We use the CRTM platform which allows us to insert various solvers for radiative transfer calculations. Three solvers mentioned above share the same atmospheric optic data, the same surface emissivity and reflectivity, and the same Planck function for atmosphere, surface, and the cosmic background. The differences of results from the three solvers are purely from the differences in the solvers. For 24,000 simulations with various clear and cloudy cases, computation times on our personal computer are 1041, 29, and 17 s for DA, VDISORT, and ADA models, respectively. ADA is about 1.7 times faster than VDISORT and 61 times faster than DA. The huge gain of ADA to DA is partly contributed by the efficiency of matrix and vector manipulation in FORTRAN 95 because DA code is still in FORTRAN 77. The maximum difference of the simulated brightness temperatures between using the three solvers for AMSU-A channels and 281 selected Atmospheric InfraRed Sounder (AIRS) channels is less than 0.01 K. The subset of AIRS data used in NCEP data assimilation contains necessary information on atmospheric temperature and water vapor (Goldberg et al. 2003). Tables 2 and 3 list the comparison of the brightness temperatures for AMSU-A water vapor channel at 23.8 GHz and the infrared window channel of AIRS at 10.88  $\mu\text{m}$  computed from ADA, VDISORT, DA methods, respectively. A profile containing temperature and water vapor as well as ozone from our test dataset for OPTRAN is selected. For the microwave calculation, a rain cloud having an effective particle size of 200  $\mu\text{m}$  and 0.5 mm rain water content was put at 850 hPa. One layer ice cloud having the same effective particle size and 0.1 mm ice water path is located at 300 hPa. A wind speed of 5  $\text{ms}^{-1}$  over ocean is used. The maximum difference of the brightness temperature computed from the three models is less than 0.01 K (see Table 2). For the infrared calculation, an ice cloud having an effective particle size of 20  $\mu\text{m}$  and 0.1 mm ice water path was located at 300 hPa and a liquid water cloud at 850 hPa having an effective particle size of 10  $\mu\text{m}$  and 0.5 mm are chosen. The results computed from the three models agree very well (see Table 3).

**Table 2** Comparison of brightness temperatures at 23.8 GHz (AMSU-A channel 1) computed from advanced doubling-adding method (ADA), VDISORT, and doubling-adding method (DA)

Zenith angle	ADA	VDISORT	DA
0	272.9645	272.9656	272.9655
10	272.9358	272.9369	272.9369
20	272.8342	272.8354	272.8354
30	272.6054	272.6065	272.6064
40	272.0529	272.0542	272.0541
50	271.1577	271.1594	271.1593
65	269.0612	269.0637	269.0635

A rain cloud having an effective radius of 200  $\mu\text{m}$  and 0.5 mm water content was put at 850 hPa. One layer ice cloud having the same effective particle size and 0.1 mm ice water path is located at 300 hPa

**Table 3** Comparison of brightness temperatures at 10.88  $\mu\text{m}$  (AIRS channel 256) computed from advanced doubling-adding method (ADA), VDISORT, and doubling-adding method (DA)

Zenith angle	ADA	VDISORT	DA
0	240.7513	240.7514	240.7514
10	240.5512	240.5513	240.5512
20	239.9758	239.9757	239.9757
30	239.1067	239.1065	239.1065
40	238.0799	238.0798	238.0798
50	237.0585	237.0585	237.0585
65	235.6128	235.6129	235.6129

An ice cloud having an effective particle size of 20  $\mu\text{m}$  and 0.1 mm ice water path was located at 300 hPa and a liquid water cloud at 850 hPa having an effective particle size of 10  $\mu\text{m}$  and 0.5 mm are chosen

4.2 Atmospheric Transmittance Models

Line-by-line transmittance model performs for each absorption line. The line width is typically about  $10^{-4} \text{ cm}^{-1}$  in stratosphere and  $10^{-2} \text{ cm}^{-1}$  in low troposphere. The line-by-line calculation demands tremendous computations that are not feasible in daily operations. The model often serves as a reference for fast radiative transfer models. LBLrtm (Clough et al. 2005) is one of the best rigorous radiative transfer models for us to generate regression coefficients in the CRTM fast transmittance models. There are two fast transmittance algorithms available in the CRTM: Optical Depth in Absorber Space (ODAS) and Optical Depth in Pressure Space (ODPS); both algorithms are regression-based and differ primarily in vertical coordinates and the application of constraints to smooth vertical structures of the regression coefficients (Chen et al. 2012). The CRTM transmittance coefficients are derived by applying regression algorithms (McMillin et al. 1995) using the line-by-line (LBL) transmittances convolved with the instrument spectral response functions (SRFs) as predictands, and atmospheric state variables as predictors. The CRTM transmittance has two parts: variable gases and fixed gases. For ODAS,  $\text{H}_2\text{O}$  and  $\text{O}_3$  are

variable gases and all other gases are treated as fixed gases. For ODPS, six gases ( $\text{H}_2\text{O}$ ,  $\text{CO}_2$ ,  $\text{O}_3$ ,  $\text{N}_2\text{O}$ ,  $\text{CO}$ , and  $\text{CH}_4$ ) are variable gases and rest gases are treated as fixed gases.  $\text{H}_2\text{O}$  and  $\text{O}_3$  are mandate inputs for both ODAS and ODPS algorithms.  $\text{CO}_2$ ,  $\text{N}_2\text{O}$ ,  $\text{CO}$ , and  $\text{CH}_4$  are optional and default values from the ODPS reference profile will be used when inputs are absent. There are two specific transmittance models in the CRTM. The stratospheric sounder unit (SSU) transmittance model (Liu and Weng 2009) was developed to take the  $\text{CO}_2$  cell pressure into account. Zeeman effect is considered for microwave sounding channels that are sensitive to upper stratosphere (Han et al. 2007). Figure 2 is the measured (forest green color)

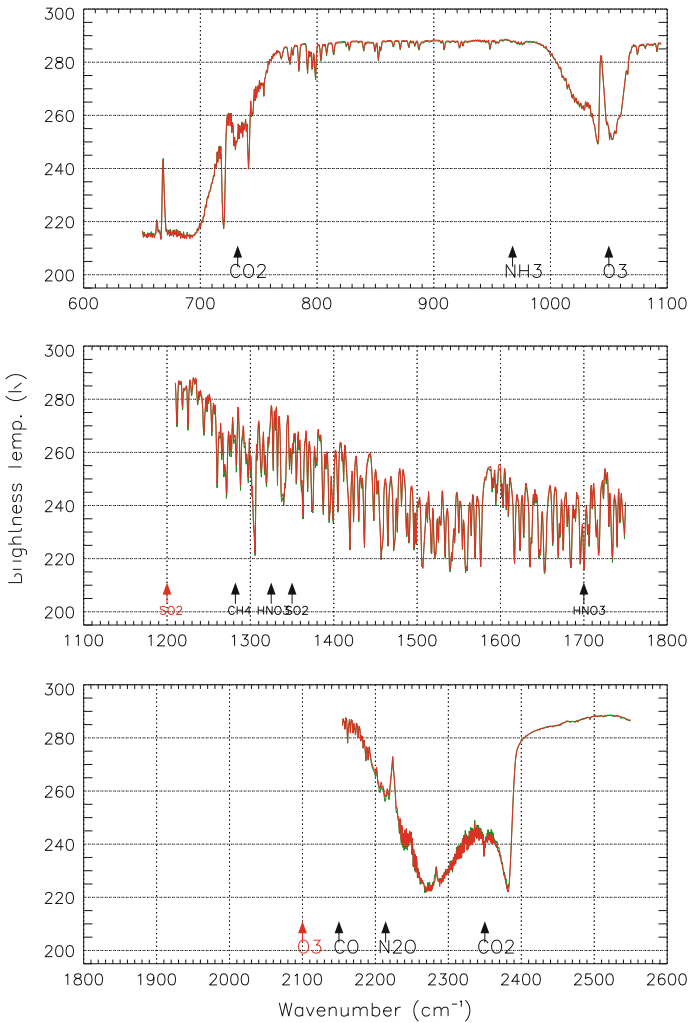


**Fig. 2** Measured (red line) and the CRTM simulated (forest green line) CrIS brightness temperatures. The upward arrows indicate the spectral absorption of gases

and the CRTM simulated (red) CrIS brightness temperature of a full spectral resolution over ocean under a clear-sky condition. In the CRTM calculation, radiosonde data and ozonesonde data from the surface to 10 hPa, and from ship measured skin temperatures are used. Above 10 hPa, the ECMWF analysis data are used. Because there was a dry bias in radiosonde water vapor in the upper troposphere during the daytime, we use the ECMWF data for water vapor above 300 hPa. We use the mean value of the ECMWF and ship measured skin temperatures as the surface temperature. Other trace gases such as CO<sub>2</sub>, N<sub>2</sub>O, CH<sub>4</sub>, and CO are taken from a standard tropic atmosphere. The CrIS brightness temperatures are calculated from Hamming apodized radiances at 2211 channels. In general, both measured and simulated CrIS brightness temperatures agree very well. Figure 1 shows main absorption of gases. CrIS observations can be used to retrieve H<sub>2</sub>O, O<sub>3</sub>, CO<sub>2</sub>, N<sub>2</sub>O, CO, CH<sub>4</sub>, NH<sub>3</sub>, SO<sub>2</sub>, and HNO<sub>3</sub>.

There is a spectral gap between long-wave band and middle-wave band, as well as a gap between mid-wave band and shortwave band. The spectral information there can help the retrieval of SO<sub>2</sub> and volcanic ash.

### 4.3 Scattering Properties

The scattering of electromagnetic wave by atmospheric particles depends on dielectric constant of particles, particle size distributions, and particle shapes and orientations. In the CRTM, we deal with spherical particles and nonspherical particles with a random orientation. The assumption is common and can simplify the optical properties to a scalar extinction and scattering coefficients and to four phase function elements for spheres and six phase function elements for nonspherical particles with a random orientation. Dielectric constant depends on electromagnetic wavelength and may also depend on temperature. Electromagnetic spectrum of sensors onboard satellites covers ultraviolet (0.20–0.38  $\mu\text{m}$ ), visible (violet (0.38–0.45  $\mu\text{m}$ ), blue (0.45–0.495  $\mu\text{m}$ ), green (0.495–0.570  $\mu\text{m}$ ), yellow (0.57–0.59  $\mu\text{m}$ ), orange (0.59–0.62  $\mu\text{m}$ ), red (0.62–0.75  $\mu\text{m}$ ), near-infrared (0.75–3.0  $\mu\text{m}$ ), infrared (3.0–50.0  $\mu\text{m}$ ), and microwave (1000–30,000  $\mu\text{m}$ ) ranges. This partition of the spectrum is approximate since different communities may have own definition (<https://en.wikipedia.org/wiki/Infrared>).

The ratio of particle diameter to electromagnetic wavelength is one of the key parameters determining scattering. The diameter of a molecule is about  $10^{-4}$   $\mu\text{m}$ . The diameter of aerosols may change from 0.1 to 10  $\mu\text{m}$ . The diameter of clouds varies from 10 to 10,000  $\mu\text{m}$ . Once the dielectric constant and particle size distribution are known, we can use Mie code to compute optical properties such as extinction coefficient, single-scattering albedo, and phase function for spherical particles.

## 4.4 *Molecules*

The diameter of molecules in the atmosphere is much smaller than the electromagnetic wavelength in our studies. The scattering by molecules is referred as the Rayleigh scattering. The optical properties of molecular scattering are referred to the literature (Mishchenko et al. 2006).

## 4.5 *Aerosols*

Aerosols are small solid or liquid particles in the atmosphere, which can be classified into primary and secondary groups. Primary aerosols, including elemental carbon, organic carbon, sea salt, and mineral dust, are emitted directly from anthropogenic and natural sources, while secondary aerosols, such as sulfate, nitrate, ammonia, and secondary organic carbon, are formed through photochemical, gaseous, aqueous, and heterogeneous chemical reactions in the atmosphere. Aerosols can influence climate directly by scattering and absorbing solar or infrared radiation. They also have impact on climate indirectly by serving as cloud condensation nuclei and ice nuclei and consequently changing albedo and lifetime of clouds.

There exist complex interactions between chemistry, aerosols, and climate. Aerosols are formed through different chemical reactions, and in turn they have impact on photochemical reactions and involve in heterogeneous chemical reactions. Aerosols can modify the global energy balance and lead to climate change, while climate change can affect concentrations of gas phase species and aerosols by changing oxidation capacity of the atmosphere as well as processes of transport, diffusion, deposition, scavenging, and mixing. The chemistry–aerosol–climate interactions play important roles in air pollution, climate change, and water cycle. There are big challenges in understanding the mechanisms of such interactions and in representing aerosols in global and regional climate models. Satellite measurements, in particular multisensor and multichannel measurements, provide useful information about aerosol types and concentrations, which may determine aerosol sources/plumes for regional and weather air quality forecasting. Current satellite aerosol optical depth (AOD) product is helpful, but not accurate to predict aerosol in boundary layer, which is the most important layer to air quality where human breath.

Due to different requirements and heritage from various communities, the calculations of optical properties are not unique, which leads to nonunique results in retrievals and assimilation. We may roughly divide the community as model groups and remote sensing groups. The Goddard Chemistry Aerosol Radiation and Transport (GOCART) model (Chin et al. 2002) is mainly used in a global model. CMAQ focus more on regional area. MODIS-like aerosol is often used in remote sensing group. The CRTM has the optical table for GOCART model for the

spectrum from ultraviolet to infrared. The effect of aerosols on microwave sensors is not considered yet since aerosol size is generally much smaller than microwave length. The optical table for CMAQ is not finalized yet. In this paper, we discuss mainly on the GOCART model.

The GOCART model simulates major tropospheric aerosol components, including sulfate, dust, black carbon (BC), organic carbon (OC), and sea salt aerosols. The sea salt has four sub-types from small particle to large particle. Anthropogenic emission of sulfate ( $\text{SO}_2$ ) from fossil fuel and biofuel combustions and transportations is taken from the Emission Data Base for Global Atmospheric Research (EDGAR) (Olivier et al. 1994). Biomass burning emission of  $\text{SO}_2$  is scaled to the seasonal variations of burned biomass data (Duncan et al. 2003). Volcanic emission of  $\text{SO}_2$  is from continuously erupting volcanoes and sporatically erupting volcanoes (when data available). Oceanic emission of dimethyl sulfide (DMS) is calculated based on the surface seawater concentrations of DMS and 10-m winds over the ocean using an empirical formula (Liss and Merlivat 1986). Dust particles ranging from 0.1 to 10  $\mu\text{m}$  in radius are considered in the model with eight size groups (0.1–0.18, 0.18–0.3, 0.3–0.6, 0.6–1, 1–1.8, 1.8–3, 3–6, and 6–10  $\mu\text{m}$ ). The biomass burning emissions of OC and BC are estimated from the database of seasonal and interannual variations in the burned biomass (Duncan et al. 2003), developed from long-term satellite observations of global fire counts and aerosol index and an annual mean burned biomass inventory. Anthropogenic emissions of OC and BC are taken from a global dataset (Cooke et al. 1999). In addition to direct emissions, the production of OC from terrestrial source is estimated from the emission of volatile organic compounds (Guenther et al. 1995). Sea salt emission from the ocean is highly dependent on the surface wind speed.

Aerosol particle size distribution plays an important role in calculating the optical properties of aerosols. In this study, we assumed a spherical aerosol particle. The aerosol size distribution may have multiple modes. For each mode, a typical aerosol size function is assumed to be the lognormal distribution (d’Almeida 1991; Han et al. 2007) for  $N$  particles within the mode,

$$n(\ln r) = \frac{N}{\sqrt{2\pi} \ln(\sigma_g)} \exp \left[ -\frac{1}{2} \left( \frac{\ln r - \ln r_g}{\ln(\sigma_g)} \right)^2 \right], \quad (18)$$

where  $r$  is a radius,  $r_g$  the geometric median radius, and  $\sigma_g$  the geometric mean standard deviation. The  $k$ th moment of the distribution can be expressed as (Binkowski and Roselle 2003)

$$M_k = \int_{-\infty}^{\infty} r^k n(\ln r) d \ln(r) = r_g^k \exp \left[ \frac{k^2}{2} \ln^2(\sigma_g) \right]. \quad (19)$$



$M_0$  is the number  $N$  of aerosol particles.  $M_2$  and  $M_3$  are proportional to the total particulate surface area and volume, respectively. Thus, the effective radius ( $r_{\text{eff}}$ ) can be defined as

$$r_{\text{eff}} = \frac{M_3}{M_2} = r_g \exp\left[\frac{5}{2} \ln^2(\sigma_g)\right]. \tag{20}$$

Table 4 lists the size parameters and computed mass extinction coefficients used in the CRTM. For sulfate, sea salt, hydrophilic OC and BC, water uptake effect needs to be included. The particle size increases as the relative humidity (RH) of ambient atmosphere increases. The reflective index needs to be calculated by considering water content in aerosols. The effective radius growth factor for hygroscopic aerosols may be theoretically calculated or obtained from a precalculated lookup table (Chin et al. 2002). Once the growth factor  $a_g$  is evaluated, the refractive index  $n$  for the hygroscopic aerosol can be calculated using a volume mixing method as

$$n_r = n_w + (n_o - n_w) \times a_g^3, \tag{21}$$

where  $n_o$  and  $n_w$  are the refractive indices for dry aerosols and water, respectively. We adopt refractive index  $n_o$  from the software package of Optical Properties of Aerosols and Clouds (OPAC) (Hess et al. 1998). The water refractive index is given by Hale and Querry (1973).

**Table 4** Goddard Chemistry Aerosol Radiation and Transport (GOCART) aerosol optical properties at 550 nm for dry air

Aerosol type	Density [g cm <sup>-3</sup> ]	Effective radius [μm]	Standard deviation σ [μm]
Sulfate	1.7	0.242	2.03
OC1 (hydrophobic)	1.8	0.087	2.20
OC2 (hydrophilic)	1.8	0.087	2.20
BC1 (hydrophobic)	1	0.036	2.0
BC2 (hydrophilic)	1	0.036	2.0
SeaSalt1 (size range)	2.2	0.3	2.03
SeaSalt2	2.2	1.0	2.03
SeaSalt3	2.2	3.25	2.03
SeaSalt4	2.2	7.5	2.03
Dust1 (size range)	2.6	0.65	2.0
Dust2	2.6	1.4	2.0
Dust3	2.6	2.4	2.0
Dust4	2.6	4.5	2.0
Dust5	2.6	8.0	2.0

Hydrophilic aerosol particle size increases as the ambient humidity increases

After the size distribution and refractive index are computed, we apply Mie code to compute mass extinction coefficient ( $\text{m}^2 \text{g}^{-1}$ ), single-scattering albedo, and phase function. Finally, AOD for each aerosol type  $i$  at the  $j$ th atmospheric layer for a wavelength  $\lambda$  can be calculated as

$$\tau_{ij}(\lambda) = \text{ext}(\lambda, i, r_{\text{eff}}) \times c_{ij}, \quad (22)$$

where  $c_{ij}$  is aerosol column mass in  $\text{g/m}^2$  for an aerosol type  $i$  and an atmospheric layer  $j$ . It can be seen from Eq. (22) that the AOD depends linearly on the layer column aerosol mass. The column total AOD is a sum of Eq. (22) over all aerosol types and atmospheric layers.

## 4.6 Clouds

Cloud particle size changes from micrometer to centimeter. The particle size affects emission and scattering of electromagnetic waves from ultraviolet to microwave. In the CRTM, we deal with six cloud types: liquid, ice, hail, graupel, and snow corresponding to the densities in  $\text{g cm}^{-3}$  of 1.0, 0.9, 0.9, 0.4, and 0.1, respectively. Liquid clouds (water and rain) are assumed to be spherical water droplet and follow the size distribution given by Hansen and Travis (1974):

$$n(r) = r^{(1-3b)/b} e^{-r/ab}, \quad (23)$$

where  $r$  is the radius of the water cloud particle,  $a$  is the effective radii, and  $b$  is the effective variance. The single-scattering properties of water droplets, including the asymmetry factor, single-scattering albedo, extinction efficiency, and scattering phase function, are computed from the Lorenz–Mie program developed by Wiscombe (Wiscombe 1980). Nonspherical particles are used for solid clouds: ice, snow, graupel, and hail. The CRTM adopted the lookup table of optical properties at the microwave range from Liu (2008) and the lookup table given by Yang et al. (2005) for ultraviolet, visible, and infrared spectrum. Table 5 lists cloud size parameters that are used for calculation size distributions of spherical particles.

## 4.7 Surface Reflectivity and Emissivity Models

The surface emissivity/reflectance models are divided into water, land, ice, and snow gross types for visible, infrared, and microwave sensors. Each gross type is further divided into subtypes, for example, new and old snows. For infrared and visible spectrum, the ASTER spectral library (Baldrige et al. 2009) data is applied for land infrared emissivity and the surface is assumed as Lambertian and the emissivity equals one minus reflectivity (Vogel et al. 2011). We also developed

**Table 5** Cloud size parameters used for calculating cloud size distributions

Type	Density g cm <sup>-3</sup>	MW $r_{\min} = 0.1 \text{ }\mu\text{m}, r_{\min} = 8000 \text{ }\mu\text{m}$			IR/VIS/UV $r_{\min} = 0.1 \text{ }\mu\text{m}, r_{\min} = 500 \text{ }\mu\text{m}$		
		Variance of size	Sphere	Nonsphere	Variance of size	Sphere	Nonsphere
Liquid	1.0	0.12 (stratocumulus)	Yes		0.12 (stratocumulus)	Yes	
Rain	1.0	1/3 (Marshall–Palmer) (Liu and Boukabara 2014)	Yes		1/3 (Marshall–Palmer)	Yes	
Ice	0.916	0.18 Nov. 1 cirrus	Yes		0.18 Nov. 1 cirrus	Yes	
Snow	0.1	1/3 (Marshall–Palmer)		Yes	1/3 (Marshall–Palmer)	Yes	
Graupel	0.4	1/3 (Marshall–Palmer)		Yes	1/3 (Marshall–Palmer)	Yes	
Hail	0.916	1/3 (Marshall–Palmer)		Yes	0.1		Yes

utility codes for users to use emissivity atlas that depends on month and latitude and longitude. The infrared water emissivity is based on Wu–Smith model (Van Delst and Wu 2000). The infrared water bidirectional reflectance distribution function (BRDF) model is used for the CRTM direct reflectance to compute reflected solar radiation. The solar radiation over sunglint area may contribute 30 K to infrared channel at 3.7  $\mu\text{m}$ . Microwave water emissivity can be calculated from surface temperature, wind vector, and salinity (Liu et al. 2011). For a calm water surface, surface emissivity is well described by Fresnel equations, as a function of temperature and salinity for a given frequency and a zenith angle. Surface wind generates surface roughness and foam that affect surface emissivity. Both a physical land surface emissivity (Weng et al. 2001) and atlas technique are available in the CRTM. In addition to the physical and atlas emissivity models, surface emissivity over snow and ice surface can be estimated from satellite measured brightness temperature inside the CRTM. The purpose of this model is to use satellite measurements at a few window channels to estimate snow or ice emissivity at those frequencies first, then predict emissivity of sounding channels for those that are also affected by surface emission (Yan et al. 2008).

5 Aerosol Models

A chemical transport model (CTM) is a numerical model that simulates the entire cycle for the species of interest, considering emissions, chemical production and loss, transport and mixing, as well as wet and dry removal. CTMs can be classified accordingly to their species of interest (e.g., aerosol models and dust models), their methodology (e.g., Eulerian models and Lagrangian models), their model characteristics (global models and regional models), as well as their integration strategy

(e.g., offline models whose chemistry is run after the meteorological simulation is done and online models that allow interactive coupling of chemistry and meteorological processes).

This section summarizes the characteristics of two aerosol prediction models that are run in an operational or pseudo-operational manner at NOAA National Centers for Environmental Prediction (NCEP). This chapter is not intended to provide a comprehensive summary of aerosol prediction models running at operational, quasi-operational, or research mode at various operational centers and research institutes around the world. The descriptions of the two aerosol models aim to put CRTM's air quality applications into the contexts.

### ***5.1 Goddard Chemistry Aerosol Radiation and Transport Model (GOCART)***

Funded mainly by NASA Earth Science programs, the Goddard Chemistry Aerosol Radiation and Transport model (GOCART) was developed to simulate atmospheric aerosols (including sulfate, black carbon (BC), organic carbon (OC), dust, and sea salt), and sulfur gases (Colarco et al. 2010; Chin et al. 2000, 2003, 2004, 2007, 2009; Ginoux et al. 2001, 2004; Janjic 2003; Bian et al. 2010; Kim et al. 2013).

Aerosol species are assumed to be external mixtures. Total mass of sulfate and hydrophobic and hydrophilic modes of carbonaceous aerosols are tracked, while for dust and sea salt the particle size distribution is explicitly resolved across five noninteracting size bins for each. Both dust and sea salt have dynamic (wind speed dependent) emission functions, while sulfate and carbonaceous species use emission inventory from fossil fuel combustion, biomass burning, and biofuel consumption, with additional biogenic sources of organic carbon. Sulfate has additional chemical production from oxidation of  $\text{SO}_2$  and DMS, and a database of volcanic  $\text{SO}_2$  emissions and injection heights is used. Aerosol sinks include wet removal (scavenging and rainout) and dry deposition (gravitational sedimentation and surface uptake).

Originally, GOCART was developed as an offline CTM, driven by assimilated meteorological fields from the Goddard Earth Observing System Data Assimilation System [GEOS DAS, e.g., Chin et al. (2002)]. As part of the GEOS Version 4 (GEOS-4) atmospheric model development at NASA Global Modeling and Assimilation Office (GMAO), an online version of GOCART has been developed (Colarco et al. 2010) and was later implemented into NCEP's global model (Lu et al. 2013). When running within versions 4 and 5 of GEOS (GEOS-4/5), the GOCART module provides aerosol processes such as emissions, sedimentation, dry and wet depositions (Fig. 3). Advection, turbulent, and convective transport is outside the GOCART module, being instead provided by the host atmospheric model. Unlike offline CTM, this online aerosol module accurately utilizes winds,

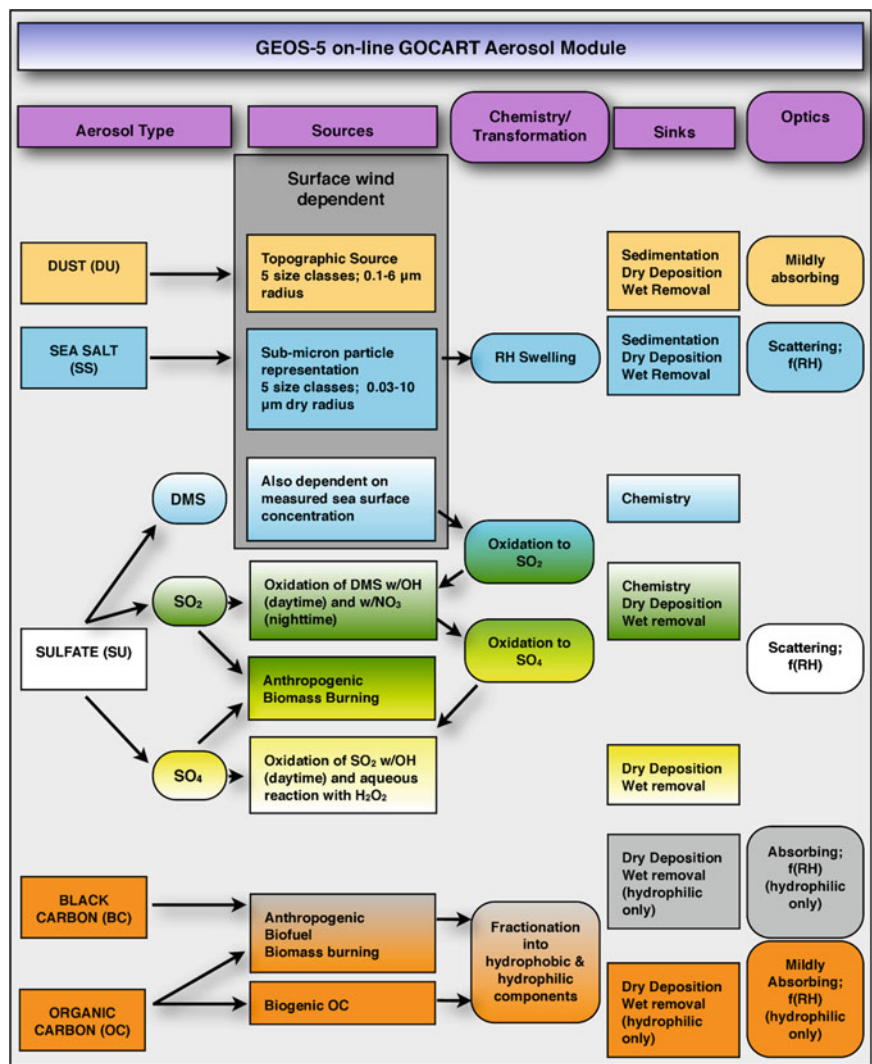


**Fig. 3** Schematic summary of the GOCART aerosol modules as adapted and being implemented in GEOS-4/5 at GMAO and NEMS GFS at NCEP

convective mass flux, and eddy diffusivity valid at each time step, without the need for temporal or spatial interpolation of any kind.

Recent research and development efforts have further enhanced GOCART modeling capabilities. The transition to online modeling mentioned above is an example. In addition, the GOCART module now has the option to ingest daily biomass burning emissions from the Quick Fire Emission Dataset (Darrenov and da Silva 2013). QFED emissions are based on fire radiative power retrievals from

MODIS (Moderate Resolution Imaging Spectroradiometer, on board Aqua and Terra satellites). The inclusion of such observation-based, time-dependent emissions is important for model to capture the large temporal–spatial variation of biomass burning emissions.

The GOCART module is currently used in the GEOS-5 Near-Real-Time (NRT) aerosol forecasting system as well as the Modern Era Retrospective analysis for Research and Applications Aerosol Reanalysis (Buchard et al. 2014). At NCEP, the GOCART module is coupled with NCEP’s meteorological model for global dust forecasts (described in Sect. 5.3) and an upgrade for multispecies forecast (including dust, sea salt, sulfate, and carbonaceous aerosols) is planned in 2015.

## 5.2 *The Community Multi-scale Air Quality (CMAQ) Modeling System*

The U.S. Environmental Protection Agency (EPA) has established National Ambient Air Quality Standards (NAAQS), requiring the development of effective emissions control strategies for pollutants such as ozone, particulate matter (PM), and nitrogen species. To meet the emission regulation needs, EPA developed the Community Multi-scale Air Quality (CMAQ) system to develop emission control strategies.

CMAQ is a state-of-the-science “one-atmosphere” system that treats major atmospheric and land processes (e.g., advection, diffusion, nucleation, coagulation, wet and dry deposition, gas phase chemistry, gas–particle mass transfer, and aqueous phase chemistry) for a range of species (e.g., anthropogenic and biogenic, primary and secondary, gaseous and particulate) in a comprehensive framework. The science, model engineering concepts, and infrastructure design have been well documented (Byun et al. 1995a, b, 1996, 1998; Ching et al. 1995; Coats et al. 1995; Byun and Schere 2006).

The CMAQ system framework is comprised of three major modeling systems: emission projection and processing system, the meteorological modeling system, and the CTM. The CMAQ CTM is used to simulate multiple pollutants with emissions and meteorological input data. The science options for CMAQ include the gas phase mechanism, PM module, a set of chemical solvers, various options for vertical and horizontal advection, and photolysis rate calculations.

In response to congressional mandate, NOAA and EPA formed a partnership to transfer scientific advances in air quality modeling at EPA into NCEP’s operational model suite. The real-time air quality forecasting system based on CMAQ will be discussed in Sect. 5.4.

### 5.3 *Global Modeling: GOCART in NEMS GFS Aerosol Component (NGAC)*

The online version of GOCART module developed for GEOS-4/5 is fairly independent of the host meteorological model, encapsulating the basic aerosol production and loss functionality. It has been incorporated into NOAA Environmental Modeling System (NEMS) to establish the first interactive global aerosol forecasting system, NEMS GFS Aerosol Component (NGAC), at NCEP (Lu et al. 2010, 2013).

The rationale for developing the global aerosol forecasting capabilities at NOAA includes: (1) to improve weather forecasts and climate predictions by taking into account of aerosol effects on radiation and clouds; (2) to improve assimilation of satellite observations by properly accounting for aerosol effects; (3) to provide aerosol (lateral and upper) boundary conditions for regional air quality predictions; (4) to provide a first step toward aerosol data assimilation and reanalysis; and (5) to produce quality aerosol information that address societal needs and stakeholder requirements, e.g., UV index, air quality, ocean productivity, visibility, and sea surface temperature retrievals.

Effective on September 11, 2012, starting with the 0000 Coordinated Universal Time (UTC) cycle, NCEP begins to run and disseminate data from the NGAC version 1 (NGAC V1) at T126 L64 resolution ( $\sim 100$  km). It provides 5-day dust forecasts, once per day for the 0000 UTC cycle. Dust initial conditions are taken from the 24-h NGAC forecast from previous day while meteorological initial conditions are downscaled from high-resolution Global Data Assimilation System (GDAS) analysis.

The NGAC V1 output is available in GRIdded Binary edition 2 (GRIB2) format on  $1 \times 1^\circ$  output grid, with 3-hourly output from 00 to 120 h. Primary output fields are global three-dimensional dust mixing ratios for five particle sizes with effective radius at 1, 1.8, 3, 6, and  $10 \mu\text{m}$ . Two-dimensional aerosol diagnosis products, such as aerosol optical depth (AOD) and surface mass concentration, are also available. The NGAC digital products can be accessed from NOMADS at <http://nomads.ncep.noaa.gov/> and NCEP's ftp server at <ftp://ncep.noaa.gov/pub/data/nccf/com/ngac>.

Figure 4 presents the evaluation of NGAC dust distributions. NGAC dust AOD has been compared to dust AOD from GEOS-5 and total AOD from MODIS onboard Terra. The source regions over the Sahara and Sahel are clearly shown as well as the patterns of long-range dust transport. Trade winds steer African dust westward across the Atlantic ocean, covering vast areas of the North Atlantic and sometimes reaching the Americas (e.g., the Caribbean, southeastern USA, Central America, and Amazon basin). This has implications for air quality, public health, climate, and biogeochemical cycle. For instance, about half of the annual dust supply to the Amazon basin is emitted from a single source in the Sahara, the Bodele depression (Koren et al. 2006).

The International Cooperative for Aerosol Prediction (ICAP), consisting of forecasting center model developers and remote sensing data providers, began



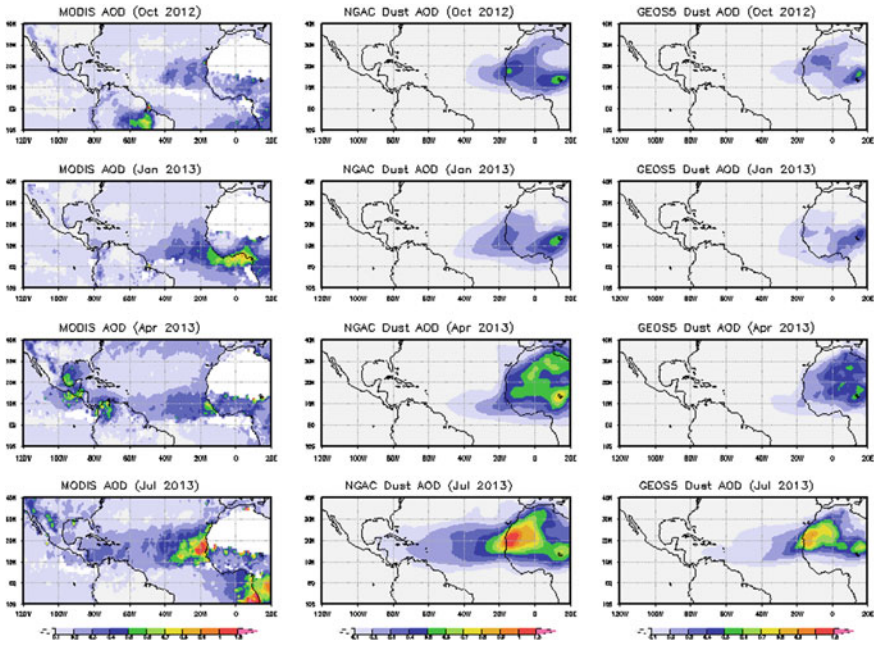


**Fig. 4** Comparisons of monthly mean MODIS total AOD (*left*), NGAC dust AOD (*middle*), and GEOS5 dust AOD (*right*) at 550 nm for 2012/10, 2013/01, 2013/04, and 2013/07 periods

meeting in April 2010 to discuss issues relevant to the operational aerosol forecasting (Benedetti et al. 2011; Reid et al. 2011). Consensus ICAP multi-model ensembles [ICAP-MME, (Sessions et al. 2015)] become pseudo-operational since 2014, using four complete aerosol forecast models from GMAO, European Centre for Medium-Range Weather Forecasts (ECMWF), Naval Research Laboratory (NRL), and Japan Meteorological Agency (JMA) as well as three dust-only models from NCEP (i.e., NGAC), U.K. Met Office (UKMO), and Barcelona Supercomputing Center (BSC). Figure 5 shows the dust AOD from ICAP-MME and NGAC, valid at 12 UTC on August 1, 2013. Spatial pattern of dust loading from NGAC is consistent with the ICAP-MME, with elevated dust located in the Sahara, the Arabian Peninsula, and Asia.

While NGAC has the capability to predict dust, sulfate, sea salt, and carbonaceous aerosols, the initial operation implementation only provides global dust forecasts. Multispecies aerosol predictions by NGAC require real-time estimates of aerosol precursor emissions. NOAA-NASA has developed global near-real-time (NRT) smoke emissions, blended from NOAA’s Global Biomass Burning Emission Product from a constellation of geostationary satellites [GBBEP, (Zhang et al. 2011)] and NASA’s Quick Fire Emissions Data from polar orbiting sensor MODIS (QFED). The NRT smoke emissions dataset is targeted to be operational in May 2015, and will be used in the planned NGAC upgrade (multispecies forecasts) slated for operation implementation in late 2015.



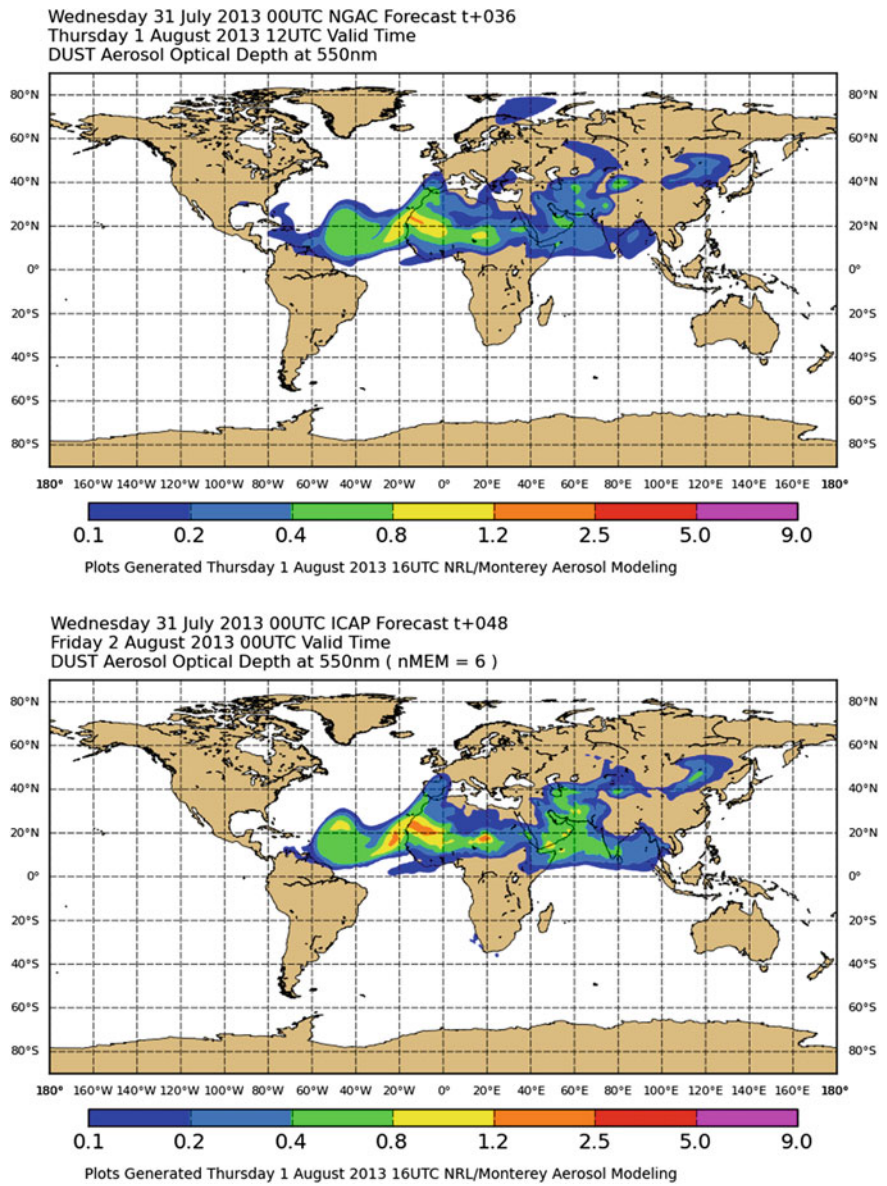


**Fig. 5** Dust AOD valid at 12UTC on August 1, 2013 for ICAP multi-model ensemble (*top*) and NGAC (*bottom*). The ensemble is based on six members, including NCEP NGAC, GMAO GEOS-5, ECMWF MACC (Monitoring Atmospheric Composition and Climate), NRL NAAPS (Navy Aerosol Analysis and Prediction System), JMA MASINGAR (Model of Aerosol Species in the Global Atmosphere), and BSC NMMB-CTM. These figures are produced by the Naval Research Laboratory

#### **5.4 Regional Modeling: CMAQ in National Air Quality Forecasting Capability (NAQFC)**

As directed by U.S. Congress, NOAA developed a National Air Quality Forecasting (AQF) System (Davidson et al. 2004) through a partnership with the U.S. EPA. The AQF system is an offline coupled atmospheric chemical forecasting system using EPA CMAQ modeling system (Ching et al. 1995), driven by meteorological forecasts from NCEP North American Mesoscale (NAM) system. The real-time U.S. National Air Quality Forecast Capability (NAQFC), based on the NAM-CMAQ system (Otte et al. 2005; Eder et al. 2010; Chai et al. 2013), run at 12 km horizontal resolution out to 48 h twice per day. The initial deployment of NAQFC covered the northeastern U.S. domain since September 2004. It was expanded to cover the eastern U.S. in August 2005 and is now extended to cover the entire continental U.S., Alaska, and Hawaii.

The NAQFC provides operational predictions of ozone from anthropogenic and natural sources since 2004. It will be upgraded to provide PM predictions in 2015. An alternative quick response model for predicting wildfire smoke and dust storms, both of which have highly variable intermittent sources, are based on the Hybrid Single Particle Lagrangian Integrated Trajectory model [HYSPLIT, (Draxler et al. 2010)] and are beyond the scope of this chapter. Descriptions of HYSPLIT smoke and dust forecast systems can be found in Eder et al. (2010) and Rolph et al. (2009), respectively.

The Carbon Bond (CB05) with 51 species and 156 reaction gas phase chemical mechanism is used operationally at NCEP (Sarwar et al. 2008). The modeling of aerosols in CMAQ is based on the PM module (AERO-IV) described in Binkowski and Roselle (2003). Secondary Organic Aerosol formation is included and described in Colarco et al. (2010). The fine PM with size is equal to or less than 2.5  $\mu\text{m}$  in diameter (PM<sub>2.5</sub>) can be predicted, speciated to nitrate, sulfate, ammonium, organics, and elemental carbon.

The Aerosol Version 4 (AERO-IV) particle model is included in the NAQFC operational configuration for aerosol chemistry. Aerosol size distributions are represented by lognormal distributions of  $\varphi$ , geometric diameter of the particles: Aitken ( $\varphi < 0.1 \mu\text{m}$ ), accumulation ( $0.1 < \varphi < 2.5 \mu\text{m}$ ), and coarse ( $2.5 < \varphi < 10 \mu\text{m}$ ). New particle formation from gas conversion and nucleation are included as well as heterogeneous hydrolysis reaction of  $\text{N}_2\text{O}_5$  (key linkage between gas and aerosol phase reactions). Predictions of organic nitrate were overpredicted in earlier configurations and influenced ozone production. As of 2015, organic nitrate is photolyzed and removed quicker by shortening lifetime by a factor of 10 based on the findings of Anderson et al. (2014) and Yang et al. (2014). Fugitive dust emissions are included and are now modulated whenever there is ice/snow to suppress emissions. Real-time wildfire smoke emissions are incorporated using the NESIDS Hazard Mapping System “observed” wildfire near-real-time smoke emissions and the U.S. Forest Service BlueSky smoke emissions system.

The emission dataset is built on top of the 2011 National Air Quality Forecasting Capability (NAQFC) baseline data, but with four major updates: (a) new point source emissions with updated emission measurements and energy projections; (b) new mobile source emissions updated to 2012 based on trends from the U.S. EPA surface monitoring network corroborated with satellite trends for the same constituents (Pan et al. 2014); (c) new off-road emissions projected to 2012; and (d) updated Canadian emission sectors from Environment Canada (EC) 2012 emission inventories and the Mexican 2010 National Inventory for Mexico. The NOAA Hazard Mapping System (HMS) is used to detect wildfires over the nation. The HMS product is then used to drive the U.S. Forest Service BlueSky wildfire emissions system. Finally, a Kalman filter-based bias correction scheme (Djalalova et al. 2015) has provided improved PM prediction skill that should result in improved guidance for State environmental agencies responsible for air quality alerts.

The NWS Air Quality Forecast Guidance, updated twice daily, is available at the NWS National Digital Graphical Database (NDGD) decision support system website (<http://airquality.weather.gov>). U.S. State and local environmental agencies use this product to issue air quality forecasts and AQI predictions in their jurisdictions. To provide the public with easy access to national air quality information, the EPA's AIRNow site (<http://www.airnow.gov>) was developed. This site provides official AQ point forecasts, issued by state and local AQ forecasters, and real-time AQI conditions.

GEOS-Chem monthly climatological gas and particle species are used at the NAM-CMAQ boundaries. The efforts to use aerosol dynamic lateral boundary conditions (LBCs) from NGAC are under way. An example on using NGAC dust information to improve air quality forecasts is presented here. Two CMAQ runs are conducted for the July 2010 period. The baseline run uses static LBCs and the experimental run uses dynamic LBCs from NGAC. Figure 6 shows the observed and modeled surface PM<sub>2.5</sub> at two AIRNOW stations in the southeast region. It is found that the incorporation of LBCs from NGAC reduces model biases and improves correlation. Clearly, the inclusion of long-range dust transport via dynamic LBCs leads to significant improvements in CMAQ forecasts during dust intrusion episodes.

## 6 Satellite Data Assimilation and Air Quality Forecasting

Aerosols play an important role in weather forecasting and climate change. Except for absorbing aerosols, aerosols reflect part of sunlight back to space. Aerosols directly affect forming clouds. The modeling and prediction of aerosols is associated with a large degree of uncertainty due to uncertainties in the emissions, transport, and its interaction with nonlinear physical processes (e.g., radiative effects, cloud and precipitation formation). Ground-based observing networks have been crucial in validating and improving our understanding of aerosol component

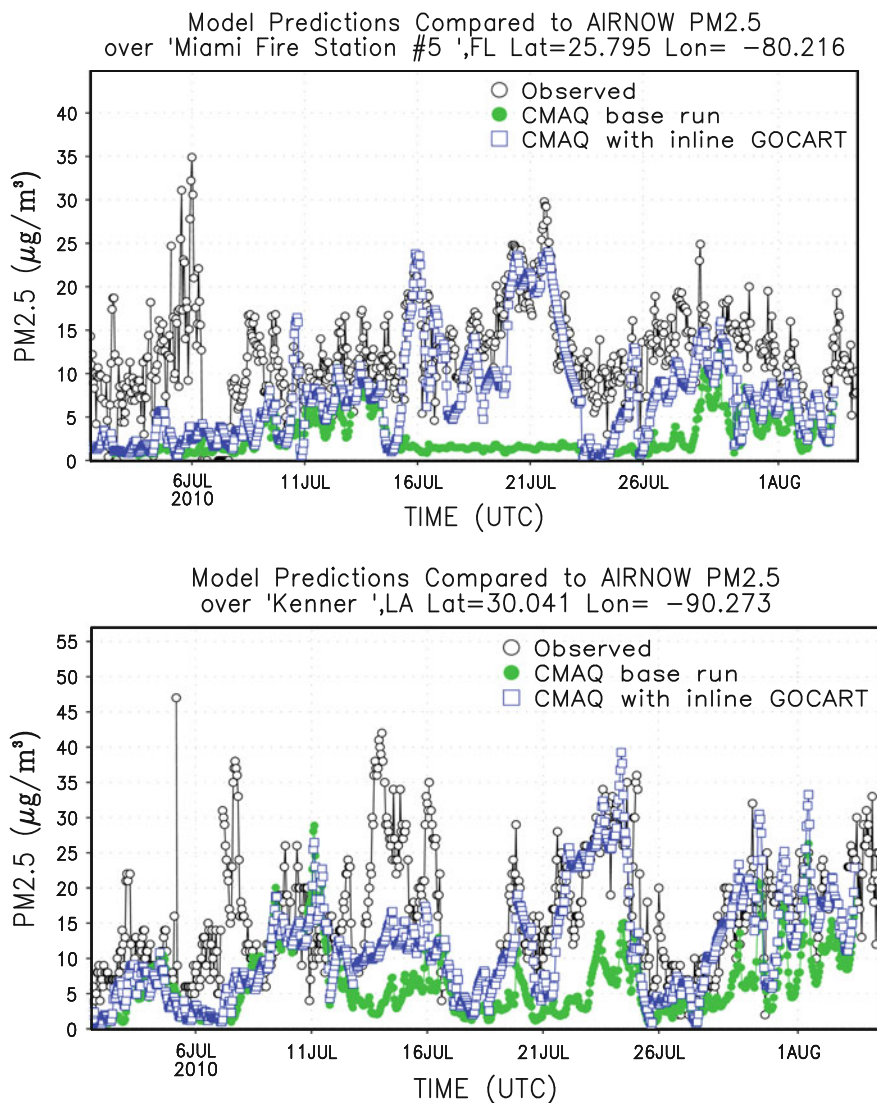


**Fig. 6** Time series of PM2.5 from EPA AIRNOW observations (*black dot*), CMAQ baseline run using static LBCs (*green dot*) and CMAQ experimental run using NGAC LBCs (*blue square*) at Miami, FL (*top panel*) and Kenner, LA (*bottom panel*)

of the entire Earth system, but the data cover a very small portion of the Earth. Complemented with ground-based networks, observations from satellite platforms offer a more global view of aerosol distribution. AVHRR (Ignatov et al. 2004), MODIS (Remer et al. 2005), VIIRS (Liu et al. 2014) provide global distribution of aerosol optical depths, which are different from aerosol mass concentration needed

by numerical forecasting model. Data assimilation system can assimilate the aerosol optical depths for aerosol mass concentrations using the CRTM. Data assimilation, an approach combining observations and information from numerical model in a statistically optimal fashion, offers a means to reduce the uncertainties in the estimates of aerosol distribution.

The Grid Statistical Interpolation (GSI) System developed at NCEP (Wu et al. 2002) is used in this study. The core of GSI is to minimize the cost function, which utilizes observations and a priori or forecast information through a 3DVAR method. The data assimilation system by minimizing the cost function finds optimal analysis fields from forecast fields, conventional observations, some retrieval products as observations, and satellite radiances under dynamic constraints following a set of physical laws. The cost function describes the departure of the solution of atmospheric/surface state parameters from background or priori information and the departure of simulations from observations. It may be written as

$$J(\mathbf{x}) = \frac{1}{2}(\mathbf{x} - \mathbf{x}_b)^T \mathbf{B}^{-1}(\mathbf{x} - \mathbf{x}_b) + \frac{1}{2}[H(\mathbf{x}) - \mathbf{y}]^T \mathbf{R}^{-1}[H(\mathbf{x}) - \mathbf{y}] \quad (24)$$

where  $\mathbf{B}$  and  $\mathbf{R}$  are the background and observation error covariance matrices of dimension  $n \times n$  and  $p \times p$ , respectively. They determine the relative weight of the background and observation term contributed to the final analysis. The superscripts “ $T$ ” and “ $-1$ ” represent, respectively, the transpose and inverse of the matrix. Here  $x$  and  $y$  are already assumed to be column vectors and hence  $J(x)$  is simply a scalar value.

Most operational NWP centers adopt an incremental implementation (Courtier et al. 1994) of Eq. (24), namely

$$J(\delta\mathbf{x}) = \frac{1}{2}\delta\mathbf{x}^T \mathbf{B}^{-1}\delta\mathbf{x} + \frac{1}{2}(\mathbf{H}\delta\mathbf{x} - \mathbf{d})^T \mathbf{R}^{-1}(\mathbf{H}\delta\mathbf{x} - \mathbf{d}) \quad (25)$$

where the analysis is based upon “increment”  $\delta\mathbf{x} = \mathbf{x} - \mathbf{x}_b$ , and the departure of observation minus background (also referred to as “innovation vector”)  $\mathbf{d} = \mathbf{y} - H(\mathbf{x}_b)$ .  $\mathbf{H}$  is the linearized version (or Jacobian, a  $p \times n$  matrix) of the nonlinear observation operator  $H$  in the vicinity of  $\mathbf{x}_b$ . The cost function in Eq. (25) is quadratic with respect to  $\delta\mathbf{x}$  and thus leads to a faster convergence of a minimization algorithm. More importantly, it allows multiple “outer loops” at lower model resolution for each loop, which is crucial to reduce computational expense in its 4DVAR implementation. At minimum of  $J(\delta\mathbf{x})$ , the gradient (the first-order partial derivative) of

$J(\delta\mathbf{x})$  with respect to  $\delta\mathbf{x}$  needs to be vanished, i.e.,

$$\nabla J_{\delta\mathbf{x}} = \mathbf{B}^{-1}\delta\mathbf{x} + \mathbf{H}^T \mathbf{R}^{-1}(\mathbf{H}\delta\mathbf{x} - \mathbf{d}) = 0. \quad (26)$$

In Eq. (5), the background and observation error covariance matrices  $\mathbf{B}$  and  $\mathbf{R}$  are determined offline. In addition to the AOD forward model, the Jacobian of



AOD with respect to aerosol mass concentration is also derived, which is required to calculate the gradient of the cost function (see Eq. 26) in the 3DVAR analysis. In addition to AOD output for those MODIS wavelengths, the CRTM-AOD operator can also calculate AOD for certain wavelengths to validate forecasts with AERONET (500, 675, 870, 1020, and 1640 nm) and CALIOP (532 nm).

The AOD observation operator is based upon the community radiative transfer model (Liu and Weng 2006) developed at the United States Joint Center for Satellite Data Assimilation (JCSDA). CRTM was primarily designed for computing satellite radiances and is used in GSI for directly assimilating radiances from infrared and microwave sensors. However, we extended CRTM to compute MODIS AOD using only aerosol profiles as input. This newly developed CRTM-AOD module was incorporated into the GSI system. Some implementations are ongoing to include WRF-Chem and CMAQ aerosol types.

In CRTM, a lookup table is necessary to store the precalculated aerosol optical parameters such as mass extinction coefficient, single-scattering albedo, and asymmetry factor.

Aerosol data assimilation using AVHRR AOD product into a three-dimensional chemical transport model was introduced by Collins et al. (2001) for studying the INDOEX (Indian Ocean Experiment) aerosols. Liu et al. (2011) used the CRTM in the GSI to assimilate MODIS aerosol optical depths to improve initial fields of aerosol mass concentration.

They adopt the total aerosol mixing ratio as control variable and some assumptions are made in order to partition the total mass into individual species (Benedetti et al. 2009). Its application to a 2-year (2003, 2004) reanalysis using MODIS AOD data showed that the analysis is very skillful in drawing to the observations and in improving the forecasts of AOD.

Experiments with and without the AOD DA have been conducted to evaluate the impact of AOD observations on the aerosol analyses and forecasts of a dust storm period (0000 UTC, 17 ~ 0000 UTC on March 24, 2010) over East Asia. Prior to running the AOD DA experiment, the corresponding background error covariance (BEC) statistics of 14 aerosol species were obtained using traditional “NMC” method, in which the difference of 24-h and 12-h WRF/Chem aerosol forecasts valid at the same time are used for BEC statistics. For the experiment without the AOD DA, aerosol fields are produced by continuous WRF/Chem forecasts driven by GFS meteorological fields and surface emission. AOD DA experiment updates aerosol fields at 0000 and 0600 UTC (day time) when the MODIS has coverage over East Asia. In Fig. 7, the hourly WRF/Chem model output is compared to the independent AOD (1020 nm) observations at two AEROSOL ROBOTIC NETWORK (AERONET) sites (Nanjing of China and Kathmandu of Nepal) for the experimental period. The noDA (green line) experiment severely underestimated AOD. The AOD values from the DA experiment (blue line) agree much more closely with AERONET observations (red line). Maximum dust intensity on March 21, 2010 in Nanjing was well captured by the AOD DA experiment. For Kathmandu site, which was unaffected by the dust storm, the diurnal variation of AOD in the AERONET

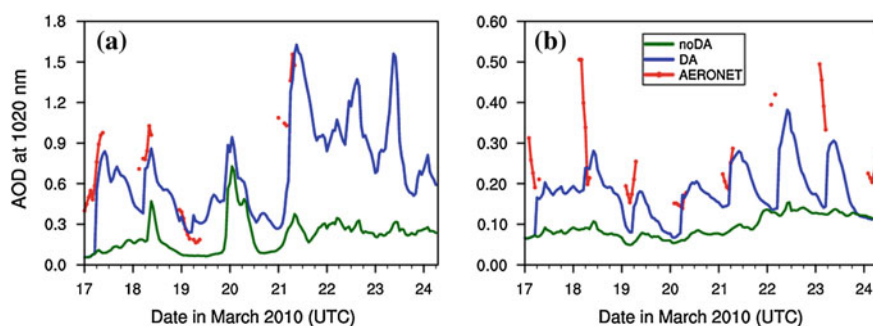


**Fig. 7** Hourly time series of AOD at 1020 nm from 0000 UTC 17 to 0600 UTC on March 24, 2010, at Nanjing and Kathmandu AERONET sites. Red line denotes the AERONET observations, and blue (green) curves represent the DA (noDA) experiment, respectively

observations, and replicated by the DA experiment, likely reflects diurnal changes in air quality caused by traffic from morning to evening.

The developed AOD assimilation method can be expanded to assimilate additional aerosol-related observations (e.g., surface measurements of particle matter, multispectral and multi-angle AOD retrievals from different satellite instruments, vertical extinction profiles from ground-based and space-borne Lidar, etc.). Moreover, 3DVAR approach adopted here permits simultaneous assimilation of new aerosol-related data and existing meteorological observations, which are already used in the GSI operation.

Air quality depends on the concentration of trace gases, for example, carbon monoxide is one of the main pollutants. Carbon monoxide is a “combustion pollutant” that comes from incomplete burning carbon materials such as vehicles running, wildfires, and biomass burning emission. Trace gases retrieved from satellite measurements are useful to determine gaseous emission sources. As shown in Fig. 1, CO absorption lines locate between 1150 and 2210  $\text{cm}^{-1}$  and observed radiance can be used to derive CO concentration. Hyperspectral infrared sounding IASI data have been used to derive CO (Pommier et al. 2010). IASI, a Fourier Transform Spectrometer (FTS) records radiance measurements from the Earth’s surface and the atmosphere with a high spectral sampling of 0.25  $\text{cm}^{-1}$  over a spectral range from 645 to 2760  $\text{cm}^{-1}$ , and with a low radiometric noise (0.2–0.35 K at 280 K reference). AIRS data are also used to derive trace gases (Susskind et al. 2003). Based on the AIRS team algorithm (Susskind et al. 2003), the NOAA developed the NOAA Unique CrIS/ATMS Processing System (NUCAPS). The NUCAPS was initially for Suomi NPP CrIS/ATMS sensors and late extends for AIRS and IASI. The description of the AIRS science team algorithm is referred to the paper (Susskind et al. 2003). It needs to be pointed out that the NUCAPS uses the microwave radiative transfer of Rosenkranz (2001) and the Stand-alone AIRS Radiative Transfer Algorithm (SARTA) (Susskind et al. 2003) is used for infrared radiance calculations. Both CRTM and SARTA are channel-based fast radiative transfer models. The NUCAPS algorithm contains two retrieval parts: microwave

(MW) data only, and infrared data with microwave data (IR + MW). The microwave only retrieval (Rosenkranz 2001) can be carried out for all-sky except for strong precipitation cases (Boukabara et al. 2007). The NUCAPS microwave retrieval convergent rate is typically higher than 96 %. Infrared retrieval of atmospheric states is a high nonlinear problem (Larrabee Strow et al. 2003). For retrieval using infrared with microwave data, the first guess plays an important role because of strong nonlinearity of the retrieval problem. We developed two regression algorithms to derive profiles of temperature, water vapor, ozone, surface temperature (Goldberg et al. 2003), and surface infrared emissivity (Zhou et al. 2008). The infrared land surface emissivity may have a large variability (Zhou et al. 2011). The first algorithm is applied for original satellite measurements for all-sky conditions. The regression coefficients are obtained by mapping ECMWF atmospheric state vectors with satellite radiances directly. The second regression algorithm is applied for clear-sky conditions. The NUCAPS algorithm is applied to each field of regard (FOR) of CrIS data where each FOR contains nine (3 × 3) field of view (FOV) in order to collocate with the ATMS measurements. At nadir looking, each CrIS FOV has a footprint of about 14 km in diameter and each CrIS FOR has a spatial resolution of about 45 km. It can be found from Table 6 that the percentage for clear-sky and overcast within FOV is much higher than within FOR. The smaller the footprint, the larger the percentage for clear and overcast scenes. The high percentage is good for clear-sky radiance and cloudy radiance assimilations. The NUCAPS IR + MW retrievals are basically called “clear-sky” retrieval where clear-sky radiances are used. In order to estimate the percentage of clear-sky conditions we collocate the CrIS FOV and FOR with the VIIRS cloud masks (Kopp et al. 2014). The VIIRS data have a good spatial resolution better than 1 km at nadir (Cao et al. 2013). For one-day global data on May 12, 2014, only 3.3 % is found clear for FORs and 8.6 % is found clear for FOVs. The low percentage of clear-sky radiances caused incomplete information content over some meteorologically very important areas and biasing the model (representative of a clear-sky only issue). To enhance the percentage of IR + MW retrieval, the NUCAPS removes cloud effects from partial cloudy scene, so-called cloud cleared radiance. Cloud cleared radiance technique has been developing and is being used in research communities and satellite retrieval products for decades. The method is applied to remove the cloud effect on radiances for partially cloudy FOV or FOR (Liu et al. 2009). The “clear-sky” radiances availability can be increased from originally 3 % to nearly 70 % for the FOR approach. The NUCAPS algorithm uses stepwise approach to retrieve geophysical parameters sequentially: temperature, water vapor, and ozone. Then the NUCAPS calculates the

**Table 6** The data percentage within CrIS field of view (FOV) and field of regard (FOR)

	Clear	1–10	10–20	20–30	30–40	40–50	50–60	60–70	70–80	80–90	90–99	100 % cloud
FOV	8.61	13.92	6.16	5.67	4.52	3.94	3.68	3.80	4.32	8.66	18.28	18.44
FOR	3.30	13.78	7.16	6.78	5.86	5.47	5.33	5.53	6.14	8.52	21.99	10.24

The spatial resolution for FOV and FOR at a nadir looking are about 14 and 45 km, respectively



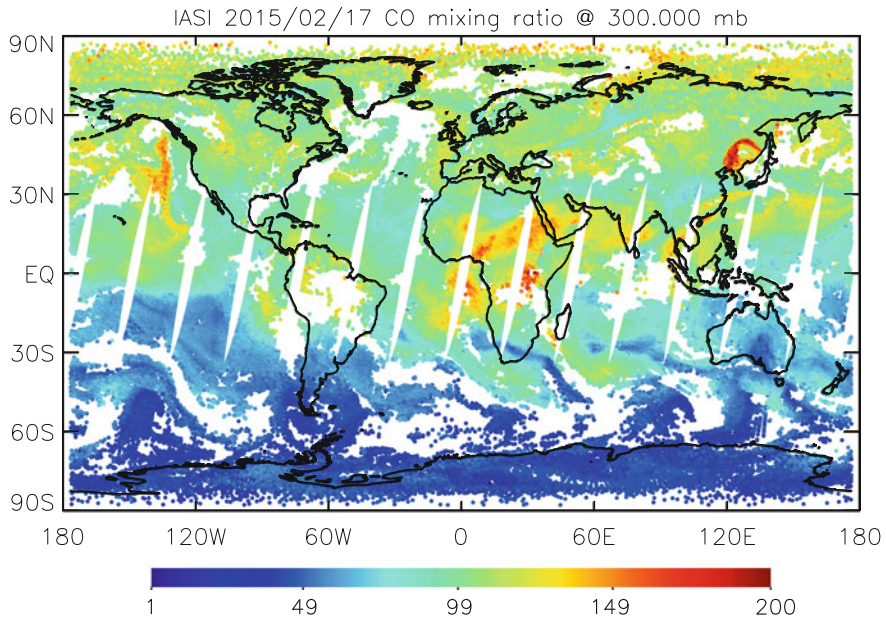


**Fig. 8** A global daily carbon monoxide EDR generated by NUCAPS for the IASI measurements

residual between measured and simulated radiances for trace gas sensitive channels (Gambacorta et al. 2014). The residual is used to estimate the concentration of trace gases without changing surface temperature and atmospheric profiles of temperature, water vapor, and ozone.

Figure 8 displayed the global concentration distribution of carbon monoxide from NUCAPS retrieval using the IASI data at ascending and descending orbits, respectively. The IASI data have a good spectral resolution that is particular interesting for retrieving trace gases. One can see high CO concentration located in Southeast Asia and central Africa. The high concentration over Northwest Pacific indicated that CO may transport to northern America.

## 7 Discussion

This chapter described the Community Radiative Transfer Model (CRTM). The CRTM and Radiative Transfer for TOVS [RTTOV] (Saunders et al. 1999) are the two operational models used for radiance assimilation in supporting of weather forecasting. The CRTM aerosol module has been used in assimilating aerosol optical depth from satellite products and improved air quality forecasting skill (Liu et al. 2011). In this study, we assimilate column aerosol optical depth at the wavelength of 0.55  $\mu\text{m}$ . The vertical distribution of aerosol concentration and

particle size is essential to the aerosol transport. Aerosols of small sizes at high altitude have a large chance to transport a long distance. Since backscattered radiances depend on wavelengths, aerosol optical depths at multiple wavelengths may provide information about the vertical distribution of aerosol concentrations and sizes. It needs to point out that the aerosol definition between the model groups and remote sensing teams may be different. The model group uses aerosol concentrations and particle sizes what dynamic models deal with. The remote sensing team uses optical properties what sensors measure. Even within model community aerosol definition can be different, for example, the size bin of dust is different in the GOCART and the CMAQ models. It is also true within remote sensing community since the retrieval of the aerosol optical depth depends on the assumptions of aerosol type, size, and concentration. Certainly, there is a good correlation between the retrieved aerosol optical depth and the aerosol concentration. To enhance the correlation, the model groups and the remote sensing teams may work together on the common aerosol definition.

The NUCAPS system retrieved trace gases using the IASI data and will generate the trace gaseous EDRs using the CrIS data of a full spectral resolution. The CrIS radiance of a full-spectral resolution is analytically scalable and derivable using fast Fourier transform. The scalable and derivable spectra may provide an additional way to the applications of remote sensing. The spectral resolution is critical to obtain necessary sensitivity of radiances on trace gaseous concentrations. The satellite products provide global distributions of aerosol optical depths and trace gases such as CO and O<sub>3</sub>. The data are useful to determine the initial field needed by prediction models. But, the aerosol optical depth represents the column value instead of a vertical distribution. The NUCAPS does provide the vertical distribution of trace gases, but the sensitivity of radiances on trace gases near surface boundary layer is low. From the spectral weighting functions of the IASI and the CrIS, we can see that the most satellite information about trace gases come from the atmospheric layers between 300 and 700 hPa. To improve the retrieval product, good priori information about trace gases is important. Within the data assimilation system, one can integrate broad information from model estimate, ground measures, and satellite radiances. The aerosol vertical distribution may be obtained from aerosol optical depths at multiple wavelengths and at multiple view angles instead of using the optical depth at a single wavelength only. The sensitivity of satellite radiance or reflectance depends on the wavelength. More studies are definitely needed to how to utilize satellite products and how to know the uncertainty of the products for each measurement. The errors estimate will allow users to determine the usage of the products for various applications.

Today's computation capability is large, but it is still not large enough to deal with each gaseous absorption line and strong scatterings of aerosols and clouds. Polarization from clouds and aerosols are not considered because of the shortage of computation capability in an operational system. The errors induced by neglect of the polarization in radiance calculations can be significant [several percents, (Mishchenko et al. 1994)] at UV and visible bands and at microwave frequencies

for some applications. The effect is relatively small at infrared wavelengths. The errors can be as large as 2 K in microwave brightness temperatures (Liu and Simmer 1996). Surface emissivity models are important in radiative transfer calculations. The uncertainties of the surface emissivity model can be large and degrade the usefulness of image channels that observe surfaces. Multiple scattering calculations can be expensive. With scatterings, radiance calculations may demand several to hundred times more computations than that without scatterings. For operational radiative transfer models, optimizing code and algorithm may not have a big room. We probably need to use advanced technology. GPU may be one of the options that can do designed calculations. It is a known fact that solving linear equations and matrix manipulations including eigenvalue problems are most time-consuming. Therefore, one can focus on those codes for GPU without changing other codes.

**Acknowledgments** The manuscript contents are solely the opinions of the authors and do not constitute a statement of policy, decision, or position on behalf of NOAA or the U.S. government.

## References

- Alvarado MJ, Wang C, Prinn RG (2009) Formation of ozone and growth of aerosols in young smoke plumes from biomass burning: 2. Three-dimensional Eulerian studies. *J Geophys Res* 114:D09307. doi:[10.1029/2008JD011186](https://doi.org/10.1029/2008JD011186)
- Anderson DC, Loughner CP, Weinheimer A, Diskin G, Canty TP, Salawitch RJ, Worden H, Fried A, Mikoviny T, Wisthaler A, Dickerson RR (2014) Measured and modeled CO and NO<sub>y</sub> in DISCOVER-AQ: an evaluation of emissions and chemistry over the eastern US. *Atmos Environ* 96:78–87
- Baldrige AM, Hook SJC, Grove I, Rivera G (2009) The ASTER spectral library version 2.0. *Remote Sens Environ* 113:711–715. doi:[10.1016/j.rse.2008.11.007](https://doi.org/10.1016/j.rse.2008.11.007)
- Benedetti A et al (2009) Aerosol analysis and forecast in the European centre for medium-range weather forecasts integrated forecast system: 2. Data assimilation. *J Geophys Res* 114:D13205. doi:[10.1029/2008JD011115](https://doi.org/10.1029/2008JD011115)
- Benedetti A, Reid JS, Colarco PR (2011) International cooperative for aerosol prediction (ICAP) workshop on aerosol forecast verification. *Bull Am Meteor Soc* 92:ES48–ES53. doi:[10.1175/BAMS-D-11-00105.1](https://doi.org/10.1175/BAMS-D-11-00105.1)
- Bian H, Chin M, Kawa SR, Yu H, Diehl T (2010) Multi-scale carbon monoxide and aerosol correlations from MOPITT and MODIS satellite measurements and GOCART model: implication for their emissions and atmospheric evolutions. *J Geophys Res* 115:D07302. doi:[10.1029/2009JD012781](https://doi.org/10.1029/2009JD012781)
- Binkowski FS, Roselle SJ (2003) Models-3 community multiscale air quality (CMAQ) model aerosol component, 1 model description. *J Geophys Res* 108:4183. doi:[10.1029/2001JD001409](https://doi.org/10.1029/2001JD001409)
- Boukabara S, Weng F, Liu Q (2007) Passive microwave remote sensing of extreme weather events using NOAA-18 AMSUA and MHS. *IEEE Geosci Remote Sens* 45:2228–2246
- Buchard V, da Silva A, Colarco P, Darmanov A, Govindaraju R, Spurr R (2014) Using OMI aerosol index and aerosol absorption optical depth to evaluate the NASA MERRA aerosol reanalysis. *Atmos Chem Phys Discuss* 14:32177–32231

- Byun DW, Schere KL (2006) Review of the governing equations, computational algorithms, and other components of the Models-3 community multiscale air quality (CMAQ) modeling system. *Appl Mech Rev* 59:51–77
- Byun DW, Hanna A, Coats CJ, Hwang D (1995a) Models-3 air quality model prototype science and computational concept development. Transactions of air & waste management association specialty conference on regional photochemical measurement and modeling studies, San Diego, CA, pp 197–212, 8–12 Nov 1993
- Byun DW, Coats CJ, Hwang D, Fine S, Odman T, Hanna A, Galluppi KJ (1995b) Prototyping and implementation of multiscale air quality models for high performance computing. Mission earth symposium, Phoenix, AZ, pp 527–532, 9–13 Apr 1993
- Byun DW, Dabdub D, Fine S, Hanna AF, Mathur R, Odman MT, Russell A, Segall EJ, Seinfeld JH, Steenkiste P, Young J (1996) Emerging air quality modeling technologies for high performance computing and communication environments. In: Gryning SE, Schiermeier F (eds) Air pollution modeling and its application XI, pp 491–502
- Byun DW, Ching JKS, Novak J, Young J (1998) Development and implementation of the EPA models-3 initial operating version: community multi-scale air quality (CMAQ) model: twenty-second NATO/CCMS international technical meeting on air pollution modelling and its application. In: Gryning SE, Chaumerliac N (eds) Air pollution modeling and its application XII. Plenum Publishing Corporation, Berlin, pp 357–368
- Cao C, Xiong J, Blonski S, Liu Q, Uprety S, Shao X, Bai Y, Weng F (2013) Suomi NPP VIIRS sensor data record verification, validation, and long-term performance monitoring. *J Geophys Res Atmos* 118 (2013) doi:[10.1002/2013JD020418](https://doi.org/10.1002/2013JD020418)
- Chai T, Kim H-C, Lee P, Tong D, Pan L, Tang Y, Huang J, McQueen J, Tsidulko M, Stajner I (2013) Evaluation of the United States National Air Quality Forecast Capability experimental real-time predictions in 2010 using air quality system ozone and NO<sub>2</sub> measurements. *Geosci Model Dev* 6:1831–1850. doi:[10.5194/gmd-6-1831-2013](https://doi.org/10.5194/gmd-6-1831-2013)
- Chen Y, Weng F, Han Y, Liu Q (2008) Validation of the community radiative transfer model (CRTM) by using cloudsat data. *J Geophys Res* 113:D00A03. doi:[10.1029/2007JD009561](https://doi.org/10.1029/2007JD009561)
- Chen Y, Han Y, Weng F (2012) Comparison of two transmittance algorithms in the community radiative transfer model: application to AVHRR. *J Geophys Res* 117:D06206. doi:[10.1029/2011JD016656](https://doi.org/10.1029/2011JD016656)
- Chin M, Savoie DL, Huebert BJ, Bandy AR, Thornton DC, Bates TS, Quinn PK, Saltzman ES, De Bruyn WJ (2000) Atmospheric sulfur cycle in the global model GOCART: Comparison with field observations and regional budgets. *J Geophys Res* 105:24689–24712
- Chin M, Ginoux P, Kinne S, Torres O, Holben BN, Duncan BN, Martin RV, Logan JA, Higurashi A, Nakajima T (2002) Tropospheric aerosol optical thickness from the GOCART model and comparisons with satellite and sunphotometer measurements. *J Atmos Sci* 59:461–483
- Chin M, Ginoux P, Luchesi R, Huebert B, Weber R, Anderson T, Masonis S, Blomquist B, Bandy A, Thornton D (2003) A global aerosol model forecast for the ACE-Asia field experiment. *J Geophys Res* 108:8654. doi:[10.1029/2003JD003642](https://doi.org/10.1029/2003JD003642)
- Chin M, Chu DA, Levy R, Remer LA, Kaufman YJ, Holben BN, Eck T, Ginoux P (2004) Aerosol distribution in the northern hemisphere during ACE-Asia: results from global model, satellite observations, and sunphotometer measurements. *J Geophys Res* 109:D23S90. doi:[10.1029/2004JD004829](https://doi.org/10.1029/2004JD004829)
- Chin M, Diehl T, Ginoux P, Malm W (2007) Intercontinental transport of pollution and dust aerosols: implications for regional air quality. *Atmos Chem Phys* 7:5501–5517
- Chin M, Diehl T, Dubovik O, Eck TF, Holben BN, Sinyuk A, Streets DG (2009) Light absorption by pollution, dust and biomass burning aerosols: a global model study and evaluation with AERONET data. *Ann Geophys* 27:3439–3464
- Ching JKS, Byun DW, Hanna A, Odman T, Mathur R, Jang C, McHenry J, Galluppi K (1995) Design requirements for multiscale air quality models. Mission earth symposium, Phoenix, AZ, pp 532–538, 9–13 Apr 1995

- Clough SA, Shephard MW, Mlawer EJ, Delamere JS, Iacono MJ, Cady-Pereira K, Boukabara S, Brown PD (2005) Atmospheric radiative transfer modeling: a summary of the AER codes. *J Quant Spectrosc Radiat Transf* 91:233–244. doi:[10.1016/j.jqsrt.2004.05.058](https://doi.org/10.1016/j.jqsrt.2004.05.058)
- Coats CJ, Hanna AH, Hwang D, Byun DW (1995) Model engineering concepts for air quality models in an integrated environmental modeling system. Transactions of air & waste management association specialty conference on regional photochemical measurement and modeling studies, San Deigo, CA, pp 213–223, 8–12 Nov 1993
- Colarco P, da Silva A, Chin M, Diehl T (2010) Online simulations of global aerosol distributions in the NASA GEOS-4 model and comparisons to satellite and ground-based aerosol optical depth. *J Geophy Res* 115:D14207. doi:[10.1029/2009JD012820](https://doi.org/10.1029/2009JD012820)
- Collins WD, Rasch PJ, Eaton BE, Khattatov BV, Lamarque J-F (2001) Simulating aerosols using a chemical transport model with assimilation of satellite aerosol retrievals: Methodology for INDOEX. *J Geophys Res* 106:7313–7336. doi:[10.1029/2000JD900507](https://doi.org/10.1029/2000JD900507)
- Cooke WF, Lioussse C, Cachier H, Feichter J (1999) Construction of a  $1^\circ \times 1^\circ$  fossil fuel emission data set for carbonaceous aerosol and implementation and radiative impact in the ECHAM4 model. *J Geophys Res* 104:22137–22162
- Courtier P, Thépaut J-N, Hollingsworth J (1994) A strategy for operational implementation of 4D-Var, using an incremental approach. *Q J R Meteorol Soc* 120:1367–1387. doi:[10.1002/qj.49712051912](https://doi.org/10.1002/qj.49712051912)
- d’Almeida GA (1991) Atmospheric aerosols, A. Deepak Publishing, Hampton
- Darmenov A, da Silva AM (2013) The quick fire emissions dataset (QFED)—documentation of versions 2.1, 2.2 and 2.4, NASA technical report series on global modeling and data assimilation. NASA TM-2013-104606, vol 32, pp 1–183
- Davidson PM, Seaman N, Schere K, Wayland RA, Hayes JL, Carey KF (2004) National air quality forecasting capability: first steps toward implementation. In: Proceedings of sixth conference on atmospheric chemistry, American Meteorological Society, Seattle, WA (Paper J2.10)
- Ding S, Yang P, Weng F, Liu Q, Han Y, van Delst P, Li J, Baum B (2011) Validation of the community radiative transfer model. *J Q S Spectrosc Radiat Transf* 112:1050–1064
- Djalalova IL, Monache D, Wilczak J (2015) PM<sub>2.5</sub> analog forecast and Kalman filter post-processing for the community multiscale air quality (CMAQ) model. *Atm Envir* 108:76–87
- Draxler RR, Ginoux P, Stein AF (2010) An empirically derived emission algorithm for wind blown dust. *J Geophys Res* 115. doi:[10.1029/2009JD013167](https://doi.org/10.1029/2009JD013167)
- Duncan BN, Martin RV, Staudt AC, Yevich R, Logan JA (2003) Interannual and seasonal variability of biomass burning emissions constrained by satellite observations. *J Geophys Res* 108:4100. doi:[10.1029/2002JD002378](https://doi.org/10.1029/2002JD002378)
- Eder B, Kang D, Trivikrama Rao S, Mathur R, Yu S, Otte T, Schere K, Wayland R, Jackson S, Davidson P, McQueen J, Bridgers G (2010) Using national air quality forecast guidance to develop local air quality index forecasts. *Bull Am Meteor Soc* 91:313–326. doi:[10.1175/2009BAMS2734.1](https://doi.org/10.1175/2009BAMS2734.1)
- Evans KF, Stephens GL (1991) A new polarized atmospheric radiative transfer model. *J Quant Spectrosc Radiat Transfer* 46:413–423
- Fischer J, Grassl H (1984) Radiative transfer in an atmospheric-ocean system: an azimuthally dependent matrix operator approach. *Appl Opt* 23:1032–1039
- Gambacorta A, Barnet C, Wolf W, King T, Maddy E, Strow L, Xiong X, Nalli N, Goldberg M (2014) An experiment using high resolution NPP CrIS measurements for atmospheric trace gases: carbon monoxide retrievals impact study. *IEEE Geosci Remote Sens Lett* 11:1639–1643
- Ginoux P, Chin M, Tegen I, Prospero J, Holben B, Dubovik O, Lin S-J (2001) Sources and global distributions of dust aerosols simulated with the GOCART model. *J Geophys Res* 106:20255–20273
- Ginoux P, Prospero J, Torres O, Chin M (2004) Long-term simulation of dust distribution with the GOCART model: correlation with the North Atlantic oscillation, environ. Model Softw 19:113–128

- Goldberg M, Qu L, McMillin Y, Wolf W, Zhou L, Divakarla M (2003) AIRS near-real-time products and algorithms in support of operational weather prediction. *IEEE Trans Geosci Remote Sens* 41:379–389
- Guenther AC, Hewitt N, Erickson D, Fall R, Geron C, Graedel T, Harley P, Graedel L, Lerdau M, McKay WA, Pierce T, Scholes B, Steinbrecher R, Tallamraju R, Taylor J, Zimmerman P (1995) A global model of natural volatile organic compound emissions. *J Geophys Res* 100:8873–8892
- Hale GM, Querry MR (1973) Optical constants of water in the 200-nm to 200- $\mu$ m wavelength region. *Appl Opt* 12:555–563
- Han Y, van Delst P, Liu Q, Weng F, Yan B, Treadon R, Derber J (2006) Community radiative transfer model (CRTM)—Version 1. NOAA NESDIS Technical Report 122
- Han Y, Weng F, Liu Q, van Delst P (2007a) A fast radiative transfer model for SSMIS upper atmosphere sounding channel. *J Geophys Res* 112:D11121. doi:[10.1029/2006JD008208](https://doi.org/10.1029/2006JD008208)
- Han Y, Weng F, Liu Q, van Delst P (2007b) A fast radiative transfer model for SSMIS upper atmosphere sounding channel. *J Geophys Res* 112:D11121. doi:[10.1029/2006JD008208](https://doi.org/10.1029/2006JD008208)
- Hansen JE, Travis LD (1974) Light scattering in planetary atmospheres. *Space Sci Rev* 16 (1973):527–610
- Heidinger AK, Christopher O, Bennartz R, Greenwald T (2006) The successive-order-of-interaction radiative transfer model. Part I: model development. *J Appl Meteorol* 45:1388–1402
- Hess M, Koepke P, Schult I (1998) Optical properties of aerosols and clouds: the software package OPAC. *Bull Am Met Soc* 79:831–844
- Hu YX, Wielicki B, Lin B, Gibson G, Tsay SC, Stamnes K, Wong T (2000)  $\delta$ -Fit: a fast and accurate treatment of particle scattering phase functions with weighted singular-value decomposition least-squares fitting. *JQSRT* 65:681–690
- Ignatov A, Sapper J, Laszlo I, Nalli N, Kidwell K (2004) Operational aerosol observations (AEROS) from AVHRR/3 on board NOAA-KLM satellites. *J Atmos Oceanic Technol* 21 (2004):3–26. doi:[10.1175/1520-0426021<0003:OAOAFO>2.0.CO;2](https://doi.org/10.1175/1520-0426021<0003:OAOAFO>2.0.CO;2)
- Janjic ZI (2003) A nonhydrostatic model based on a new approach. *Meteorol Atmos Phys* 82:271–285. doi:[10.1007/s00703-001-0587-6](https://doi.org/10.1007/s00703-001-0587-6)
- Kim D, Chin M, Bian H, Tan Q, Brown ME, Zheng T, You R, Diehl T, Ginoux P, Kucsera T (2013) The effect of the dynamic surface bareness to dust source function, emission, and distribution. *J Geophys Res* 118:1–16. doi:[10.1029/2012JD017907](https://doi.org/10.1029/2012JD017907)
- Kopp TJ, Thomas W, Heidinger AK, Botambekov D, Frey RA, Hutchison KD, Iisager BD, Brueske K, Reed B (2014) The VIIRS cloud mask: progress in the first year of S-NPP toward a common cloud detection scheme. *J Geophys Res Atmos* 119:2441–2456. doi:[10.1002/2013JD020458](https://doi.org/10.1002/2013JD020458)
- Koren I, Kaufman YJ, Washington R, Todd MC, Rudich Y, Vanderlei Martins J, Resenfeld D (2006) The Bodele depressions: a single spot in the Sahara that provides most of the mineral dust to the Amazon forecast. *Environ Res Lett* 1:014005 (5pp). doi:[10.1088/1748-9326/1/1/014005](https://doi.org/10.1088/1748-9326/1/1/014005)
- Larabee Strow L, Hannon SE, De Souza-Machado S, Motteler HE, Tobin E (2003) An overview of the AIRS radiative transfer model. *IEEE Trans Geosci Remote Sens* 41:303–313
- Lee P, Liu Y (2014) Preliminary evaluation of a regional atmospheric chemical data assimilation system environmental surveillance. *Int J Environ Res Public Health* 11:12795–12816
- Liang S, Zhong B, Fang H (2006) Improved estimation of aerosol optical depth from MODIS imagery over land surfaces. *Remote Sens Environ* 104:416–425
- Liang X-M, Ignatov A, Kihai Y (2009) Implementation of the community radiative transfer model in advanced clear-sky processor for oceans and validation against nighttime AVHRR radiances. *J Geophys Res* 114:D06112. doi:[10.1029/2008JD010960](https://doi.org/10.1029/2008JD010960)
- Liou KN (2002) An introduction to atmospheric radiation, 2nd edn. Academic Press, San Diego
- Liss PS, Merlivat L (1986) Air-sea gas exchange rates: introduction and synthesis. In: Buat-Menard P (ed) *The role of air-sea exchange in geochemical cycling*. Reidel, Hingham, MA, pp 113–127



- Liu G (2008) A database of microwave single-scattering properties for nonspherical ice particles. *Bull Am Meteor Soc*. 89:1563–1570. doi:[10.1175/2008BAMS2486.1](https://doi.org/10.1175/2008BAMS2486.1)
- Liu Q, Boukabara S (2014) Community radiation transfer model (CRTM) applications in supporting the Suomi national polar-orbiting partnership (SNPP) mission validation and verification. *Remote Sens Environ* 140:744–754
- Liu Q, Ruprecht E (1996) A radiative transfer model: matrix operator method. *Appl Opt* 35:4229–4237
- Liu Q, Simmer C (1996) Polarization and intensity in microwave radiative transfer model. *Contrib Atmos Phys* 69:535–545
- Liu Q, Weng F (2006) Advanced doubling-adding method for radiative transfer in planetary atmospheres. *J Atmos Sci* 63:3459–3465
- Liu Q, Weng F (2009) Recent stratospheric temperature observed from satellite measurements. *SOLA* 5:53–56. doi:[10.2151/sola.2009-014](https://doi.org/10.2151/sola.2009-014)
- Liu Q, Weng F (2013) Using advanced matrix operator (AMOM) in community radiative transfer. *IEEE JSTAR* 6:1211–1212. doi:[10.1109/JSTARS.2013.2247026](https://doi.org/10.1109/JSTARS.2013.2247026)
- Liu Q, Xiao S (2014) Effects of spectral resolution and signal-to-noise ratio of hyperspectral sensors on retrieving atmospheric parameters. *Opt Lett* 39:60–63
- Liu Z, Vaughan M, Winker D, Kittaka C, Getzewich B, Kuehn R, Omar A, Powell K, Trepte C, Hostetler C (2009a) The CALIPSO lidar cloud and aerosol discrimination: version 2 algorithm and initial assessment of performance. *J Atmos Oceanic Technol* 26:1198–1213
- Liu X, Zhou DK, Larar AM, Smith WL, Schluessel P, Newman SM, Taylor JP, Wu W (2009b) Retrieval of atmospheric profiles and cloud properties from IASI spectra using super-channels. *Atmos Chem Phys* 9:9121–9142. doi:[10.5194/acp-9-9121-2009](https://doi.org/10.5194/acp-9-9121-2009)
- Liu Z, Liu Q, Lin HC, Schwartz CS, Lee YH, Wang T (2011a) Three-dimensional variational assimilation of MODIS aerosol optical depth: implementation and application to a dust storm over East Asia. *J Geophys Res* 116:D23206. doi:[10.1029/2011JD016159](https://doi.org/10.1029/2011JD016159)
- Liu Q, Weng F, English S (2011b) An improved fast microwave water emissivity model. *IEEE TGRS* 49:1238–1250
- Liu Q, Li C, Xue Y (2013) Sensor-based clear and cloud radiance calculations in the community radiative transfer model. *Appl Opt* 52:4981–4990
- Liu H, Remer LA, Huang J, Huang H-C, Kondragunta S, Laszlo I, Oo M, Jackson JM (2014) Preliminary evaluation of S-NPP VIIRS aerosol optical thickness. *J Geophys Res Atmos* 119 (2014):3942–3962. doi:[10.1002/2013JD020360](https://doi.org/10.1002/2013JD020360)
- Lu S, Huang H-C, Hou Y-T, Tang Y, McQueen J, da Silva A, Chin M, Joseph E, Stockwell W (2010) Development of NCEP global aerosol forecasting system: an overview and its application for improving weather and air quality forecasts. In: NATO science for peace and security series: air pollution modelling and its application vol XX, pp 451–454. doi:[10.1007/978-90-481-3812-8](https://doi.org/10.1007/978-90-481-3812-8), 2010
- Lu S, da Silva A, Chin M, Wang J, Moorthi S, Juang H, Chuang HY, Tang Y, Jones L, Iredell M, McQueen J (2013) The NEMS GFS aerosol component: NCEP's global aerosol forecast system, NCEP Office Note 472. Available at: <http://www.lib.ncep.noaa.gov/ncepofficenotes/files/on472.pdf>, Washington D.C., 26 pp
- Lu S, Iredell M, Wang J, Moorthi S, McQueen J, Chuang H-Y, Hou Y-T, Juang H, Yang W, da Silva A, Chin M (2013) The NEMS GFS aerosol component: NCEP's global aerosol forecast system, NCEP Office Note 472, 26 pp. Available at: <http://www.lib.ncep.noaa.gov/ncepofficenotes/files/on472.pdf>, Washington D.C.
- McMillin LM, Crone JJ, Goldberg MD, Kleespies TJ (1995) Atmospheric transmittance of an absorbing gas. 4. OPTRAN: a computationally fast and accurate transmittance model for absorbing gases with fixed and variable mixing ratios at variable viewing angles. *Appl Opt* 34:6269–6274
- Mishchenko MI, Lacis AA, Travis LD (1994) Errors induced by the neglect of polarization in radiance calculations for Rayleigh-scattering atmospheres. *J Quant Spectrosc Radiat Transfer* 51:491–510

- Mishchenko MI, Travis LD, Lacis AA (2006) Multiple scattering of light by particles. University Press, Cambridge
- Olivier JG, Bouwman AF, van der Maas CW, Berdowski JJ (1994) Emission database for global atmospheric research (Edgar). *Environ Monit Assess* 31:93–106. doi:[10.1007/BF00547184](https://doi.org/10.1007/BF00547184)
- Otte TL, Pouliot G, Pleim JE, Young JO, Schere KL, Wong DC, Lee PCS, Tsidulko M, McQueen JT, Davidson P, Mathur R, Chuang HY, DiMego G, Seaman NL (2005) Linking the eta model with the community multiscale air quality (CMAQ) modeling system to build a national air quality forecasting system. *Weather Forecast* 20:367–384
- Pan L, Tong D, Lee P, Kim H-C, Chai T (2014) Assessment of NO<sub>x</sub> and O<sub>3</sub> forecasting performances in the U.S. national air quality forecasting capability before and after the 2012 major emissions updates. *Atmos Environ* 95:610–619. doi:[10.1016/j.atmosenv.2014.06.020](https://doi.org/10.1016/j.atmosenv.2014.06.020)
- Plass GN, Kattawar W, Catchings FE (1973) Matrix operator theory of radiative transfer, 1: rayleigh scattering. *Appl Opt* 12:314–329
- Pommier M, Law KS, Clerbaux C, Turquety S, Hurtmans D, Hadji-Lazaro J, Coheur P-F, Schlager H, Ancellet G, Paris J-D, Nédélec P, Diskin GS, Podolske JR, Holloway JS, Bernath P (2010) IASI carbon monoxide validation over the Arctic during POLARCAT spring and summer campaigns. *Atmos Chem Phys* 10:10655–10678. doi:[10.5194/acp-10-10655-2010](https://doi.org/10.5194/acp-10-10655-2010)
- Potter P, Ramankutty N, Bennett EM, Donner SD (2010) Characterizing the spatial patterns of global fertilizer application and manure production. *Earth Interact* 14:1–22. doi:[10.1175/2009EI288.1](https://doi.org/10.1175/2009EI288.1)
- Reid JS, Benedetti A, Colarco PR, Hansen JA (2011) International operational aerosol observability workshop. *Bull Am Meteor Soc* 92:ES21–ES24. doi: [10.1175/2010BAMS3183.1](https://doi.org/10.1175/2010BAMS3183.1)
- Remer LA et al (2005) The MODIS aerosol algorithm, products, and validation. *J Atmos Sci* 62:947–973. doi:[10.1175/JAS3385.1](https://doi.org/10.1175/JAS3385.1)
- Rolph GD, Draxler RR, Stein AF, Taylor A, Ruminski MG, Kondragunta S, Zeng J, Huang H, Manikin G, McQueen JT, Davidson PM (2009) Description and verification of the NOAA smoke forecasting system: the 2007 fire season. *Weather Forecast* 24:361–378
- Rosenkranz PW (2001) Retrieval of temperature and moisture profiles from AMSU-A and AMSU-B measurements. *IEEE Trans Geosci Remote Sens* 39:2429–2435
- Sarwar G, Luecken D, Yarwood G, Whitten G, Carter B (2008) Impact of an updated carbon bond mechanism on air quality using the community multiscale air quality modeling system: preliminary assessment. *J Appl Meteorol Clim* 47:3–14
- Saunders RW, Matricardi M, Brunel P (1999) An improved fast radiative transfer model for assimilation of satellite radiance observations. *Quart J R Meteorol Soc* 125:1407–1425
- Saunders R, Brunel P, von Engeln A, Bormann N, Strow L, Hannon S, Heilliette S, Liu X, Miskolczi F, Han Y, Masiello G, Moncet JL, Uymin G, Sherlock V, Turner DS (2007) A comparison of radiative transfer models for simulating AIRS radiances. *J Geophys Res* 112: D01S90. doi:[10.1029/2006JD007088](https://doi.org/10.1029/2006JD007088)
- Schmetz J, Raschke E (1981) An approximate computation of infrared radiative fluxes in a cloudy atmosphere. *Pure appl Geophys* 119:248–258
- Seinfeld JH, Pandis SN (2006) Atmospheric chemistry and physics—from air pollution to climate change, 2nd edn. Wiley, New York
- Sessions WR, Reid JS, Benedetti A, Colarco PR, da Silva A, Lu S, Sekiyama T, Tanaka TY, Baldasano JM, Basart S, Brooks ME, Eck TF, Iredell M, Hansen JA, Jorba OC, Juang H-M, Lynch P, Morcrette J-J, Moorthi S, Mulcahy J, Pradhan Y, Razingar M, Sampson CB, Wang J, Westphal DL (2015) Development towards a global operational aerosol consensus: basic climatological characteristics of the international cooperative for aerosol prediction multi-model ensemble (ICAP-MME). *Atmos Chem Phys* 15:355–362. doi:[10.5194/acp-15-335-2015](https://doi.org/10.5194/acp-15-335-2015)
- Stamnes K, Tsay S-C, Wiscombe W, Jayaweera K (1988) Numerically stable algorithm for discrete ordinate method radiative transfer in multiple scattering and emitting layered media. *Appl Opt* 27:2502–2529



- Susskind J, Barnet CD, Blaisdell J (2003) Retrieval of atmospheric and surface parameters from AIRS/AMSU/HSB data in the presence of clouds. *IEEE Trans Geosci Remote Sens* 41:390–409
- Sutton MA, Mason KE, Sheppard LJ, Sverdrup H, Haeuber R, Hicks WK (eds) (2014) Nitrogen deposition, critical loads and biodiversity. Springer, New York
- Van de Hulst HC (1963) A new look at multiple scattering, Technical Report. Goddard Institute for Space Studies, NASA, New York
- Van Delst P, Wu X (2000) A high resolution infrared sea surface emissivity database for satellite applications. In: Technical proceedings of eleventh international ATOVS study conference, Budapest, Hungary, pp 407–411, 20–26 Sept
- Vogel R, Liu Q, Han Y, Weng F (2011) Evaluating a satellite-derived global infrared land surface emissivity data set for use in radiative transfer modeling. *J Geophys Res* 116:D08105. doi:[10.1029/2010JD014679](https://doi.org/10.1029/2010JD014679)
- Weng F, Liu Q (2003) Satellite data assimilation in numerical weather prediction models, part I: forward radiative transfer and jacobian modeling in cloudy atmospheres. *J Atmos Sci* 60:2633–2646
- Weng F, Yan B, Grody NC (2001) A microwave land emissivity model. *J Geophys Res* 106:20,115–20,123
- Wiscombe WJ (1980) Improved Mie scattering algorithms. *Appl Opt* 19:1505–1509
- Wiscombe WJ, The Delta-M Method (1957) Rapid yet accurate radiative flux calculations for strongly asymmetric phase function. *J Atmos Sci* 34:1408–1422
- Wu W-S, Purser RJ, Parrish DF (2002) Three-dimensional variational analysis with spatially inhomogeneous covariances. *Mon Weather Rev* 130:2905–2916
- Wu X, Liu Q, Zeng J, Grotenhuis M, Qian H, Caponi M, Flynn L, Jaross G, Sen B, Buss R et al (2014) Evaluation of the sensor data record from the nadir instruments of the ozone mapping profiler suite (OMPS). *J Geophys Res-ATMOS* 119:6170–6180
- Yan B, Weng F, Meng H (2008) Retrieval of snow surface microwave emissivity from the advanced microwave sounding unit. *J Geophys Res* 113:D19206. doi:[10.1029/2007JD009559](https://doi.org/10.1029/2007JD009559)
- Yang P, Wei HL, Huang HL, Baum BA, Hu YX, Kattawar GW, Mishchenko MI (2005) Fu, Scattering and absorption property database for nonspherical ice particles in the near- through far-infrared spectral region. *Appl Opt* 44:5512–5523
- Yang K, Simon A, Ge CC, Wang J, Dickerson RR (2014) Advancing measurements of tropospheric NO<sub>2</sub> from space: New algorithm and first global results from OMPS. *Geophys Res Lett* 41(2014):4777–4786. doi:[10.1002/2014GL060136](https://doi.org/10.1002/2014GL060136)
- Zhang X, Kondragunta X, Ram J, Schmidt C, Huang H-C (2011) Near-real-time global biomass burning emissions products from geostationary satellite constellation. *J Geophys Res* 117:D14201. doi:[10.1029/2012JD017459](https://doi.org/10.1029/2012JD017459)
- Zhou L, Goldberg M, Barnet C, Cheng Z, Sun F, Wolf W, King T, Liu X, Sun H, Divakarla M (2008) Regression of surface spectral emissivity from hyperspectral instruments. *IEEE Trans Geosci Remote Sens* 46:328–333
- Zhou DK, Larar AM, Liu X, Smith WL, Larrabee Strow L, Yang P, Schlüssel P, Calbet X (2011) Global land surface emissivity retrieved from satellite ultraspectral IR measurements. *IEEE Trans Geosci Remote Sens* 49:1277–1290. doi:[10.1109/TGRS.2010.2051036](https://doi.org/10.1109/TGRS.2010.2051036)

<http://www.springer.com/978-3-662-49536-0>

Light Scattering Reviews, Volume 11

Light Scattering and Radiative Transfer

Kokhanovsky, A. (Ed.)

2016, XXI, 509 p. 188 illus., 109 illus. in color.,

Hardcover

ISBN: 978-3-662-49536-0